HHS Public Access

Author manuscript

Cell Rep. Author manuscript; available in PMC 2022 September 21.

Published in final edited form as:

Cell Rep. 2022 September 06; 40(10): 111313. doi:10.1016/j.celrep.2022.111313.

Ablating Lgr5-expressing prostatic stromal cells activates the ERK-mediated mechanosensory signaling and disrupts prostate tissue homeostasis

Xing Wei[1], **Li Zhang**[1], **Yiqun Zhang**[2], **Cody Cooper**[3], **Chris Brewer**[3], **Chia-Feng Tsai**[4], **Yi-Ting Wang**[4], **Micah Glaz**[5], **Hunter B. Wessells**[1], **Jianwen Que**[6], **Mark A. Titus**[7], **Vincenzino Cirulli**[8], **Adam Glaser**[9], **Tao Liu**[4], **Nicholas P. Reder**[3], **Chad J. Creighton**[2], **Li Xin**[1,7,10,*]

[1]Department of Urology, University of Washington, 850 Republican Street, Seattle, WA 98109, USA

[2]Dan L. Duncan Comprehensive Cancer Center, Baylor College of Medicine, Houston, TX 77030, USA

[3]Alpenglow Biosciences, Inc., Seattle, WA 98103, USA

[4]Biological Sciences Division, Pacific Northwest National Laboratory, Richland, WA 99354, USA

[5]Molecular Engineering and Sciences Institute, University of Washington, Seattle, WA 98109, USA

[6]Department of Medicine, Columbia University Medical Center, New York, NY 10032, USA

[7]Department of Genitourinary Medical Oncology, MD Anderson Cancer Center, University of Texas, Houston TX 77030, USA

[8]Institute for Stem Cell and Regenerative Medicine, University of Washington, Seattle, WA 98109, USA

[9]Department of Mechanical Engineering, University of Washington, Seattle, WA 98109, USA

[10]Lead contact

SUMMARY

Functional implication of stromal heterogeneity in the prostate remains incompletely understood. Using lineage tracing and light-sheet imaging, we show that some fibroblast cells at the mouse proximal prostatic ducts and prostatic urethra highly express Lgr5. Genetic ablation of these anatomically restricted stromal cells, but not nonselective ablation of prostatic stromal cells,

*Correspondence: xin18@uw.edu.

AUTHOR CONTRIBUTIONS

Conceptualization, X.W. and L.X.; investigation, X.W., L.Z., C.C., C.B., C.-F.T., M.G., M.A.T., V.C., and A.G.; formal analysis: X.W., Y.Z., C.C., Y.-T.W., T.L., N.P.R., C.J.C., and L.X.; writing – original draft, L.X. and X.W.; writing – review & editing, L.X. with input from X.W., C.-F.T., and C.J.C.; discussion, H.B.W.; resources, J.Q.; funding acquisition, L.X.; supervision, L.X.

SUPPLEMENTAL INFORMATION

Supplemental information can be found online at https://doi.org/10.1016/j.celrep.2022.111313.

DECLARATION OF INTERESTS

The authors declare no competing interests.

rapidly induces prostate epithelial turnover and dedifferentiation that are reversed following spontaneous restoration of the Lgr5$^+$ stromal cells. RNA sequencing (RNA-seq) analysis indicates that ablating the Lgr5$^+$ stromal cells activates a mechanosensory response. Ablating the Lgr5$^+$ stromal cells impairs the control of prostatic ductal outlet, increases prostate tissue stiffness, and activates the mitogen-activated protein kinase (MAPK). Suppressing MAPK overrides the elevated epithelial proliferation. In summary, the Lgr5$^+$ stromal cells regulate prostate tissue homeostasis and maintain its functional integrity in a long-distance manner. Our study implies that the cells at organ junctions most likely control organ homeostasis by sustaining a balanced mechanoforce.

Graphical Abstract

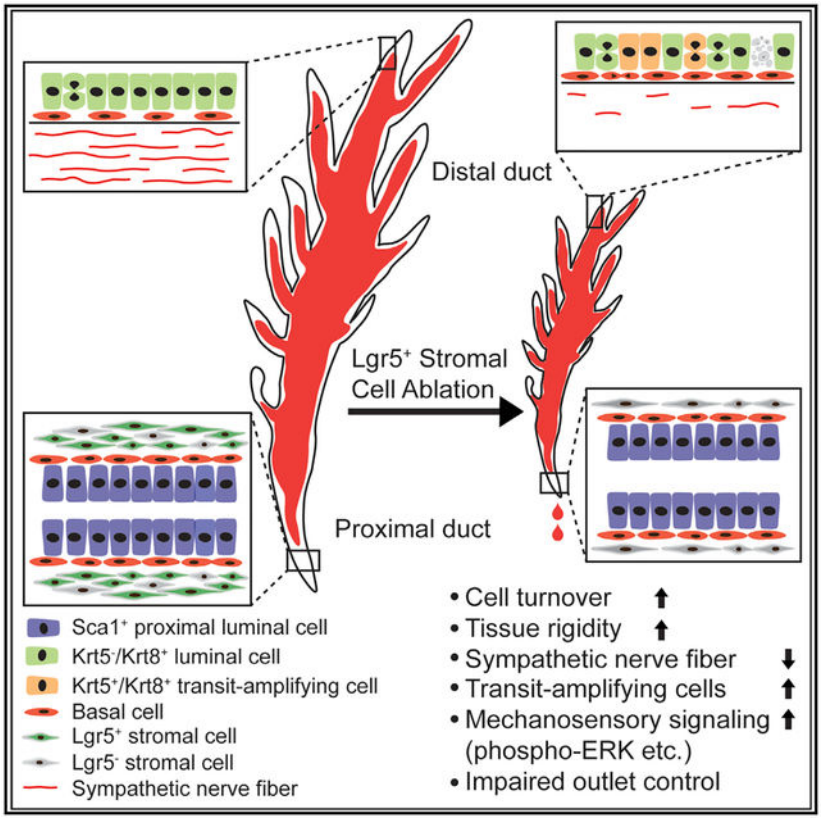

In brief

Wei et al. show that the stromal cells at the junction of mouse prostate and urethra highly express Lgr5. Genetically ablating these cells impairs the control of prostatic ductal outlet, increases prostate tissue stiffness, activates the mitogen-activated protein kinase (MAPK)-mediated mechanosensory response, and rapidly induces prostate epithelial turnover and dedifferentiation.

INTRODUCTION

Mechanotransduction is a process through which cells transduce the mechanical stimuli into a biochemical output (Chen, 2008). Cells can sense compressive, tensile, or fluid-applied forces through cell-cell and cell-extracellular matrix adhesion, which modulates

integrin signaling, alters cytoskeleton and actomyosin contractility, regulates focal adhesion assembly and disassembly, and activates mechanoresponsive signaling and the downstream effectors of mechanotransduction pathways. Cells can also sense mechanical forces via mechanosensitive ion channel or primary cilium. Mechanical forces can impact the development and morphogenesis of embryos (Vining and Mooney, 2017) and regulate stem cell fate determination and maintenance of tissue homeostasis in many organ systems (Aragona et al., 2020; Engler et al., 2006; Wu et al., 2020).

The prostate is an organ containing a fluid-filled lumen. Various physiological and pathological processes can change mechanical forces that prostate epithelial cells sense. For example, approximately 20% of prostatic fluid is expelled out of prostatic lumen during ejaculation (Zaichick and Zaichick, 2014). The smooth muscle contraction and the fluctuations in lumen pressure instigate compressive and tensile forces. In the disease settings including prostate cancer and benign prostatic hyperplasia, the development of reactive stroma and fibrosis can alter the stiffness of extracellular matrix (ECM) in the prostate (Kai et al., 2019; Rodriguez-Nieves and Macoska, 2013). The impact of altered mechanoforce on disease initiation and progression has been appreciated, but little is known regarding how the physiology-associated changes in mechanical forces affect prostate epithelial biology and tissue homeostasis.

Both mouse and human prostates sit at the base of the bladder surrounding the urethra. The mouse prostate has 4 different lobes (anterior, ventral, dorsal, and lateral lobes) containing tubular structures with lumen filled with prostatic secretions. The lining epithelium of all lobes consists of a layer of secretory luminal cells, the basal cells located beneath, and very rare neuroendocrine cells (Ittmann, 2018). The glands of each lobe are surrounded by stroma of different thicknesses consisting of smooth muscle cells and various fibroblasts (Kwon et al., 2019; Peng et al., 2013). Human prostate is microscopically reminiscent of the mouse prostate but is composed of 3 different glandular zones (transition, peripheral, and central zones) with lobular structures. In contrast to the relatively thin mouse prostate stroma, the human prostate glands are completely embedded in thick fibromuscular stroma with abundant smooth muscle cells and fibroblasts.

The prostate gland opens into the urethra. The mouse prostatic ducts adjacent to the urethra are called proximal prostatic ducts, in contrast to the rest of the ducts termed distal prostatic ducts (Tsujimura et al., 2002). We and others have shown that both epithelial and stromal cells at the proximal ducts are distinct from those at the distal ducts. The proximal epithelial cells expressing the Sca-1 surface antigen serve as the ductal epithelial cells and exhibit a higher facultative stem or progenitor activity in various *in vitro* and *in vivo* assays (Kwon et al., 2016, 2020; McAuley et al., 2019; Sackmann-Sala et al., 2014). The stromal cells in this region not only highly express versatile Wnt ligands including Wnt5a but also exhibit a strong canonical Wnt activity, which collectively keep the proximal epithelial cells in a replication quiescent state (Wei et al., 2019). In this study, genetic ablation of the Lgr5-expressing proximal stromal cells provided us a serendipitous opportunity to evaluate how changes in mechanoforce affect prostate biology that is otherwise difficult to study because natural changes in mechanoforce in the prostate are often transient and hard to capture. We demonstrate that these stromal cells are distinct from the stromal cells in the

other prostatic regions in that they regulate prostate tissue homeostasis in a long-distance manner by maintaining anatomic integrity.

RESULTS

The Lgr5$^+$ stromal cells reside at the proximal ducts of mouse prostate

We showed previously that the stromal cells at the mouse proximal prostatic ducts highly express *Axin2* and *Lgr5* (Wei et al., 2019), which was corroborated by a recent single cell RNA sequencing (scRNA-seq) analysis (Joseph et al., 2021). Lgr5 is a stem cell marker but was also reported to be expressed in the stromal cells in the lung (Lee et al., 2017; Zepp et al., 2017), small intestine (Bahar Halpern et al., 2020), and skin (Gur et al., 2022). The biological function of the Lgr5-expressing stromal cells in those organs is not completely understood. To characterize the distribution and identity of the Lgr5$^+$ cells in the prostate, we performed fluorescence-activated cell sorting (FACS) analysis using an *Lgr5-DTR-EGFP* mouse model in which the enhanced green fluorescent protein (EGFP) and diphtheria toxin receptor (DTR) are driven by the endogenous *Lgr5* promoter (Tian et al., 2011). Figure S1A shows the anterior (AP), dorsolateral (DLP), and ventral (VP) prostates dissected from an experimental mouse. The EGFP$^+$ cells were almost exclusively identified in the Lin$^-$Sca-1$^+$CD49f$^-$ stromal cells but not in the Lin$^-$Sca-1$^+$CD49f$^+$ basal cells, Lin$^-$Sca-1$^-$CD49f^{low} nonproximal (distal) luminal cells, Lin$^-$Sca-1$^+$CD49f^{low} proximal luminal cells, or Lin$^+$ cells (Figure 1A and S1B). These cells were enriched in the proximal ducts of all the prostatic lobes, consisting of approximately 40%–60% of the stromal cells in the proximal ducts. They were rare in the nonproximal ducts of the AP and DLP but consisted of approximately 3%–5% of the stromal cells throughout the nonproximal VP.

The EGFP expression in the *Lgr5-DTR-EGFP* mice can be detected in the small intestinal stem cells by immunostaining but is under the detection threshold in the prostate under the same condition (Figure S1C). To investigate the cellular identity of the Lgr5-expressing prostate stromal cells, we employed the *Lgr5-EGFP-IRES-CreER^{T2}* (*Lgr5-CreER^{T2}*) model (Barker et al., 2007). In the prostate of this model, the expression of EGFP is also undetectable by immunostaining (data not shown) and distinctly weaker by FACS (Figure S1D) compared with that of the strong EYFP by the *R26-LSL-EYFP* reporter allele. We generated *Lgr5-CreER^{T2};R26-LSL-EYFP* bigenic mice (hereafter referred to as *Lgr5-EYFP*) and treated them with tamoxifen to turn on EYFP in the Lgr5-expressing cells (Figure 1B). The expression of EYFP was activated specifically in the stromal cells of the proximal ducts of AP, and, on average, 18% of the stromal cells in the proximal ducts were labeled with EYFP (Figure S1D). Immunostaining confirmed that the EYFP$^+$ cells located outside the epithelial gland. These cells expressed vimentin but not α-smooth muscle actin, CD45, or CD31 (Figures 1C and S1E), demonstrating that they are fibroblast cells. Immunostaining also revealed that the Lgr5$^+$ stromal cells were present at the distal ducts of the ventral lobe (Figure S1F), corroborating the FACS analysis in Figure 1A.

Pdgfrβ-CreER^{T2} and *NG2-CreER^{T2}* are often used to label fibroblasts and pericytes, respectively. We generated a cohort of *Pdgfrβ-CreER^{T2};R26-LSL-tdTomato;Lgr5-DTR-EGFP* and *NG2-CreER^{T2};R26-LSL-tdTomato;Lgr5-DTR-EGFP* triple transgenic mice. Three days after tamoxifen treatment, we analyzed the expression of EGFP and tdTomato

in the $Lin^{-}CD24^{-}$ $CD49f^{-}$ stromal cells in proximal prostates. In the proximal prostate, *Pdgfrβ-CreER^{T2}* labeled approximately 36.7% of the stromal cells, and these cells were enriched in the region closer to the epithelia, whereas *NG2-CreER^{T2}* only labeled 1.2% of the stromal cells, which surrounded the blood vessels (Figure S1G). Figure 1D shows that the Lgr5-expressing $EGFP^{+}$ cells barely expressed tdTomato in the *NG2-CreER^{T2};R26-LSL-tdTomato;Lgr5-DTR-EGFP* mice, indicating that they are not pericytes. In contrast, 84.9% of the $EGFP^{+}$ stromal cells were also $tdTomato^{+}$ in the *Pdgfrβ-CreER^{T2};R26-LSL-tdTomato;Lgr5-DTR-EGFP* mice. Although it is unclear whether the $tdTomato^{-}$ $EGFP^{+}$ stromal cells indeed did not express *Pdgfrβ* or this reflected an incomplete tdTomato labeling by *Pdgfrβ-CreER^{T2}*, these data demonstrate that at least 84.9% of the $Lgr5^{+}$ stromal cells express *Pdgfrβ*.

To gain a more accurate and comprehensive view of the $Lgr5^{+}$ cells throughout the gland, we processed the prostate tissues of tamoxifen-treated *Lgr5-EYFP* mice using the tissue-clearing technique and evaluated the 3-dimensional distribution of the $Lgr5^{+}$ cells with a novel open-top light-sheet (OTLS) imaging technique (Glaser et al., 2019; Reder et al., 2019). OTLS imaging confirmed that the $Lgr5^{+}$ cells were enriched at the proximal ducts of APs and were rarely detected in the distal ducts (Figures 1E; Video S1). Figure 1F quantifies the distribution of the $Lgr5^{+}$ cells along the proximal-distal axis of the anterior lobe. OTLS imaging confirmed that the $Lgr5^{+}$ stromal cells also resided in the proximal ducts of dorsolateral lobes but were absent in the distal ducts (Video S2). In contrast, the $Lgr5^{+}$ stromal cells were evenly distributed in the nonproximal ducts of the VP (Figures 1G; Video S2). The $EYFP^{+}$ cells surrounded prostate tubules, extended extensively, spanned a long range along prostatic tubules, and often exhibited a spindle-like or triangular shape. Therefore, even though they only constituted 3%–5% of the stromal cells in distal ventral ducts (Figures 1A and S1F), they appeared visually abundant (Figures 1G; Video S2). Finally, the $Lgr5^{+}$ stromal cells were also enriched in the prostatic urethra but were less frequently seen in distal urethra (Video S2). Collectively, these analyses demonstrate that the $Lgr5^{+}$ fibroblast cells are enriched in the proximal ducts of the mouse prostate and prostatic urethra but are also sparsely and evenly distributed at the nonproximal ducts of the VP.

Spatiotemporally regulated Lgr5 is dispensable for prostate development

We performed an RNA *in situ* analysis to examine the expression dynamics of *Lgr5* during prostate development. Figure 2A shows that at embryonic day 15.5 (E15.5), *Lgr5* was highly expressed in both the urogenital sinus (UGS) mesenchyme and epithelia. At E18.5, the expression of *Lgr5* in UGS epithelia remained comparable to that at E15.5, but the expression in the UGS mesenchyme was upregulated. Postnatally, the $Lgr5^{+}$ stromal cells were confined at the proximal prostatic ducts (Figure 2A). At week 2 after birth, *Lgr5* was still present at a low level in the epithelial cells at the distal prostatic ducts but became almost undetectable in the distal prostatic epithelial cells at week 10 (Figure 2A). We were also able to identify the Lgr5-expressing stromal cells in the small intestine, colon, and stomach (Figure S2A).

The *Lgr5-CreER^{T2}* line is *Lgr5* haploinsufficient, so we used homozygous *Lgr5-CreER^{T2}* (*Lgr5* null) mice (Figure S2B) to determine whether *Lgr5* is crucial for the prostate

development and homeostasis. To rescue the lethality caused by *Lgr5* null, we transplanted *Lgr5*-null mouse UGS under the renal capsules of immunodeficient mice (Figure S2C). *Lgr5*-null UGS developed the same as the control wild-type UGS both in terms of growth (Figures 2B and S2D), histology (Figure S2E), and lineage marker expression (Figure S2F), although there was an increased apoptosis in the epithelial cells (Figure 2C). Collectively, these observations reveal a dynamic spatiotemporal expression pattern of *Lgr5* during prostate development and demonstrate that *Lgr5* per se is dispensable for prostate development.

Ablating Lgr5$^+$ stromal cells disrupts prostate homeostasis

To investigate the role of the Lgr5$^+$ stromal cells in prostate homeostasis, we ablated them by treating adult *Lgr5-DTR-EGFP* mice with DT (Figure 3A). We describe the changes in the biology mainly focusing on the AP lobes where the alterations were most prominent. The EGFP$^+$ Lgr5-expressing cells were effectively eliminated in the proximal ducts of AP at day 9 after DT treatment (Figures 3B and S3A). The EGFP$^+$ cells gradually recovered to 45% of the level in the control mice at week 16 post DT treatment (Figures 3B and S3A). Immunostaining revealed a drastic increase in stromal cell proliferation in proximal AP at day 3 after DT treatment (Figures S3B and S3C), suggesting that the Lgr5$^+$ stromal cells were likely sustained by duplication of the nearby stromal cells.

Figure 3C shows that the weight of anterior lobes decreased by 30% at day 9 post DT treatment, which was likely a result of shrunken lumen because the glands were less plump and translucent (Figure 3D), and epithelial cells packed tighter (Figure 3E), yet the total prostate cell number was not significantly reduced (Figure 3F). At week 16 after DT treatment, the prostate weight of *Lgr5-DTR-EGFP* mice also became comparable to that of the control mice (Figure 3C), consistent with the timeline of the restoration of the EGFP$^+$ stromal cells. At day 3 post DT treatment, there was a significant increase in epithelial proliferation throughout the gland as determined by immunostaining of Ki67 (Figure 3G). The increase in proliferation took place in both basal (Figure 3H) and luminal (Figure 3I) cells throughout the gland, although the Lgr5$^+$ cells only resided at the proximal ducts. The increased cell proliferation already peaked at day 3 post ablation of the Lgr5$^+$ stromal cells and gradually waned to a level comparable to that in the control group at week 16 post ablation (Figures 3H and 3I). There was also an apparent increase in cellular apoptosis, predominantly in the luminal cells, as determined by co-immunostaining of the cleaved caspase 3, Krt5, and Krt8 (Figure 3J). The increased apoptosis explains why the total cell number per prostate did not change significantly despite the increased cellular proliferation. More interestingly, the density of the prostatic sympathetic nerve fibers decreased dramatically as determined by immunostaining of the sympathetic nerve cell marker tyrosine hydroxylase (TH) (Figure 3K). The density of the sympathetic nerve fibers slightly decreased at day 3 post ablation and became almost undetectable at day 9 post ablation (Figure 3L). However, by week 16 post DT treatment, the expression of TH also recovered to the level comparable to that of the control (Figures 3K and 3L). Notably, the increased cell proliferation occurred prior to the depletion of the sympathetic nerve fibers, which suggests that the increased cell proliferation is unlikely a consequence of the loss of sympathetic nerve.

Ablating the Lgr5^{+} stromal cells also altered the phenotypic profiles of the prostate cell lineages. FACS analysis showed that there was an increased ratio of the Lin^{-}CD49f^{+}CD24^{Low} or Lin^{-}CD49f^{+}Sca-1^{+} basal cells versus the Lin^{-}CD49f^{Low}CD24^{+} or Lin^{-}CD49f^{Low}Sca-1$^{-/low}$ luminal cells at day 9 post ablation (Figures S3E and S3F). This is consistent with the increased apoptosis in the luminal cells (Figure 3J). Immunostaining not only confirmed the increased ratio of the basal cells but also revealed an emergence of the transit-amplifying cells (TACs) that expressed both the basal cell marker Krt5 and the luminal cell marker Krt8 at day 9 post DT treatment (Figure 3M). These TACs gradually disappeared at week 16 post DT treatment (Figure 3N).

To investigate the origin of these TACs, we generated the *Krt7-CreER^{T2};R26-LSL-EYFP;Lgr5-DTR-EGFP* and *Krt8-CreER^{T2}; R26-LSL-tdTomato;Lgr5-DTR-EGFP* triple transgenic mice (hereafter referred to as *K7-EYFP;Lgr5-DTR* and *K8-tdToma-to;Lgr5-DTR*, respectively). Different fluorescent reporters (EYFP and tdTomato) were chosen to enable optimal multiplex immunostaining using compatible antibodies of different species because we were limited to use the mouse anti-tdTomato and rabbit anti-Krt5 antibodies for specific and strong immunostaining. The *Lgr5-DTR-EGFP* allele does not interfere with the epithelial lineage tracing using the *R26-LSL-EYFP* model because *Lgr5-DTR-EGFP* only marks the stromal cells in the proximal APs. Experimental mice were treated with tamoxifen so that the Krt7-expressing basal and Krt8-expressing luminal cells were fluorescently labeled. Mice were then treated with DT to ablate the Lgr5-expressing stromal cells (Figures 4A and 4C). The expression status of tdTomato or EYFP in TACs would inform their origin. The *Krt7-CreER^{T2}* (Jiang et al., 2017) and *Krt8-CreER^{T2}* (Choi et al., 2012) lines specifically targeted the basal and luminal cells in nonproximal prostate ducts, respectively (Figures 4B and 4D). Approximately 21.6% of the EYFP-labeled cells were Krt5^{+}/Krt8^{+} TACs in the *K7-EYFP;Lgr5-DTR* mice (Figure 4B) whereas only 2.2% of tdTomato-labeled cells were TACs in the *K8-tdTomato;Lgr5-DTR* mice (Figure 4D) post treatment with tamoxifen and DT, demonstrating that the TACs were mainly derived from the basal cells. In summary, these results show that ablating the Lgr5^{+} stromal cells causes a rapid disruption of prostate tissue homeostasis and that repopulation of the Lgr5^{+} stromal cells restores the tissue homeostasis.

The phenotypes resulting from the ablation of the Lgr5^{+} stromal cells in the DLP and VP lobes were relatively moderate and somewhat different. The prostate weight and cell number of the DLP and VP were not significantly or consistently altered (Figures S4A and S4B). Both the proliferation and apoptosis in the stromal cells were transiently increased in the DLP and VP at day 3 post ablation, as demonstrated by the immunostaining of Ki67 and cleaved caspase 3 (Figures S4C and S4D, yellow arrows), whereas the epithelial cells were not significantly affected. There was no emergence of the Krt5^{+}/Krt8^{+} TACs in either DLP or VP at day 9 after DT treatment (Figure S4E). The TH^{+} sympathetic nerve fibers in both the DLP and VP were reduced but still detectable at day 9 post ablation of the Lgr5^{+} stromal cells (Figure S4F).

Ablating Lgr5$^+$ stromal cells does not disrupt prostate homeostasis via endocrine or sympathetic nervous system

Eliminating the Lgr5$^+$ stromal cells did not cause a dramatic change in the immune cell lineages within the prostate, excluding a potential role of inflammation in the dysregulated tissue homeostasis (Figures S5A and S5B). The Lgr5$^+$ stromal cells are located far away from distal ducts in the AP. However, ablating these cells caused phenotypic changes throughout the whole prostate in 3 days. This implies that the phenotypes were mediated by a mechanism that worked in a rapid long-distance manner. There are three potential such mechanisms: endocrinal, neural, and mechanosensory regulation, which we investigated individually.

The prostate is an androgen-dependent organ. Androgen deprivation can cause rapid prostate involution. We first investigated whether the phenotypes induced by the ablation of the Lgr5$^+$ stromal cells were due to altered androgen signaling. Castration did not phenocopy ablation of the Lgr5$^+$ stromal cells, as it did not induce epithelial proliferation (Figure 5A) or emergence of the Krt5$^+$/Krt8$^+$ TACs (Figure 5B), although castration reduced sympathetic nerve fibers (Figure 5C). In addition, the androgen receptor remained nuclear localized in the prostate of DT-treated *Lgr5-DTR-EGFP* mice, indicating that the androgen signaling was still intact (Figure 5D). Finally, there was no significant difference in serum testosterone level between the *Lgr5-DTR-EGFP* and control mice treated with DT (Figure 5E). Collectively, these studies support that ablating the Lgr5$^+$ stromal cells did not disrupt tissue homeostasis via the androgen-regulated signaling.

It is also unlikely that ablating the Lgr5$^+$ stromal cell disrupted epithelial homeostasis via alteration of sympathetic nerves because cell proliferation peaked before the complete loss of sympathetic nerve fiber (Figures 3H, 3I, and 3L). To directly exclude the possibility, we performed chemical sympathectomy with 6-hydroxydopamine (6-OHDA) in adult mice to determine whether it phenocopied the ablation of the Lgr5$^+$ stromal cells at day 9 after treatment. Consistent with previous studies (Ayala et al., 2001), 6-OHDA treatment eliminated prostatic sympathetic nerve fibers and marginally reduced the weight of AP (Figures 5F and 5G). However, there was no emergence of the TACs (Figure 5H), increased epithelial proliferation (Figure 5I), or apoptosis (Figure 5J). These results further support that the changes in epithelial differentiation and turnover upon ablation of the Lgr5$^+$ stromal cells are independent of the loss of sympathetic nerve.

Ablating Lgr5$^+$ stromal cells induces epithelial proliferation via the ERK mechanosensory signaling

To characterize the molecular changes induced by the ablation of the Lgr5$^+$ stromal cells, we FACS-isolated the basal, luminal, and stromal cells from APs of DT-treated *Lgr5-DTR-EGFP* and control wild-type mice and compared their gene-expression profiles by RNA-seq. We identified 841, 492, and 370 genes that were differentially expressed by at least 1.4-fold between the two groups in the basal, luminal, and stromal cells, respectively (Figure 6A; Table S1). Gene Ontology analysis (Figure 6B) reveals that the genes associated with regulation of immune system process were upregulated in the stromal cells of the Lgr5$^+$ cell ablation group, supporting a response to tissue damage

or stress. In contrast, the genes associated with neuron projection, axon guidance, blood vessel development, response to hypoxia, anatomical structure morphogenesis, and negative regulation of epithelial proliferation were downregulated in the $Lgr5^+$ cell ablation group, which is consistent with the loss of sympathetic nerve and increased epithelial proliferation. This also suggests that the loss of sympathetic nerve fibers is likely driven by the changes in the stromal cells. In the basal cells, genes associated with regulation of transport and metabolic process were downregulated in the $Lgr5^+$ cell ablation group. Genes associated with cytoskeleton organization, cadherin and laminin binding, cell-substrate adherens junctions, focal adhesion, and small GTPase binding were upregulated. These changes imply that ablating the $Lgr5^+$ cells alters mechanosensory signaling mediated through adhesion of the basal cells with ECM. Finally, in the luminal cells, the genes associated with negative regulation of the execution phase of apoptosis were decreased, which is consistent with an increased apoptosis. In addition, the genes associated with the mitochondria, oxidation-reduction process, metabolic process, Golgi, and endoplasmic reticulum parts were downregulated, implying a decreased secretory phenotype. Contrarily, the genes associated with actin filament organization, focal adhesion, adherens junctions, G-protein-coupled receptor signaling, Ras, Rac, Rho signal transduction, and mitogen-activated protein kinase kinase kinase (MAPKKK)/ERK1/ERK2 cascade were upregulated, suggesting an activation of the mechanosensory response specifically mediated through the ERK signal pathway.

Immunostaining and western blot analyses corroborated the finding from the RNA-seq analysis. Figures 6C, S6A, and S6B show that phosphorylated ERK1/2 (pERK1/2) (Thr202/Tyr204) was drastically upregulated throughout the prostatic gland at day 3 post ablation of the $Lgr5^+$ stromal cells. The phosphorylation of ERK1/2 decreased gradually to the baseline level in the control at week 16 post ablation (Figures 6C and S6C). The dynamics of signal change aligned with that of cell proliferation. Other molecules involved in the mechanotransduction signaling were not consistently or dramatically changed, including FAK, YAP, and P38 MAPK. (Figures S6A and S6B). There was a noticeable increase in the phosphorylation of JNK (Thr183/Tyr185) in the epithelial cells at day 3 after the $Lgr5^+$ stromal cell ablation, which persisted at day 9 post ablation (Figure S6D). The activation of JNK pathway was corroborated by the increased nuclear staining of phosphorylated c-Jun (Ser73) after the ablation of the $Lgr5^+$ stromal cells (Figure S6E). However, these changes could not be consistently validated by western blot analysis (Figures S6A and S6B).

ERK has been shown to be involved in cell proliferation. We sought to determine whether pharmacologically antagonizing ERK can rescue the increased proliferation induced by the loss of $Lgr5^+$ stromal cells. As shown in Figure 6D, we used trametinib to suppress ERK activation while ablating the $Lgr5^+$ stromal cells by DT treatment. Trametinib effectively suppressed ERK activation (Figures 6E and S6F) and reduced the $BrdU^+$ proliferating cells by 55% (Figure 6F) but did not affect the increased apoptosis (Figure S6G). Collectively, these results demonstrate that ablating the $Lgr5^+$ stromal cells activates the MAPK-mediated mechanotransduction signaling and promotes epithelial proliferation.

Previously, we showed that the luminal cells at proximal ducts display the features of ductal epithelial cells (Kwon et al., 2020). The function of the duct is to transport prostatic fluid

and control the fluid flow into the urethra with the support from surrounding stromal cells. We reason that eliminating the $Lgr5^+$ stromal cells in this region impairs the ductal outlet control of the prostate, reduces lumen pressure, and causes prostate tissue shrinkage, which activate mechanosensory signaling in epithelial cells, alter tissue rigidity, and trigger the phenotypes. We obtained multiple lines of evidence that support this hypothesis.

Firstly, we used a *Col1a2-CreER^{T2};R26-LSL-DTR;R26-LSL-EYFP* triple transgenic model to nonselectively ablate approximately 10% of prostate stromal cells but did not observe any of the phenotypes seen in the *Lgr5-DTR-EGFP* model (Figures S7A–S7E), suggesting that the anatomic location of the $Lgr5^+$ stromal cells is critical in inducing the phenotypes. Secondly, we reasoned that if ablating the Lgr5-expressing stromal cells impairs the outlet control of the prostatic ducts that join the urethra, more prostate-related proteins would be detected in urine. To this end, we analyzed urine and prostate fluids of wild-type (WT) mice at day 3 post DT treatment using liquid chromatography coupled to tandem mass spectrometry (LC-MS/MS) and identified 1,105 prostate-fluid-specific proteins, 322 urine-specific proteins, and 1,237 proteins shared by urine and prostate fluids (Figure 7A; Table S2). We then analyzed the urine of *Lgr5-DTR-EGFP* mice at day 3 post DT and PBS treatment using the same approach (Figure 7A). We identified 92 prostate fluid proteins that were presented only in the urine of the PBS-treated *Lgr5-DTR-EGFP* mice. In contrast, 631 prostate fluid proteins were identified in the urine of the DT-treated *Lgr5-DTR-EGFP* mice. 1,077 prostate fluid proteins were identified in the urine of both groups. However, the abundance of 143 out of 1,077 proteins (among which 891 are quantified proteins, i.e., the proteins having signal intensities in at least 3 valid values in one sample group) is much higher in the urine of the DT-treated than the PBS-treated *Lgr5-DTR-EGFP* group (Figures 7B; Table S2). Of note, 890 (809 quantified proteins) out of the 1,077 prostate fluid proteins were also detected in the urine of DT-treated WT mice. The abundance of more than 53% (n = 426) of these proteins was higher in the DT-treated *Lgr5-DTR-EGFP* group than in the DT-treated control group (Figure S7F). This indicates that the increased abundance of the prostate fluid proteins is unlikely due to the DT treatment per se but is because of the ablation of the Lgr5-expressing stromal cells. Collectively, the increased number and abundance of the prostate-related proteins in the urine support an impaired outlet control of prostate ducts in the DT-treated *Lgr5-DTR-EGFP* mice. Thirdly, using atomic force microscopy, we showed that the distal prostate lobes became stiffer (a 3-fold increase in elastic modulus) after the $Lgr5^+$ stromal cells were ablated (Figure 7C). Finally, electron microscopy revealed that the luminal cells of the control prostate glands exhibited normal content of clear secretory vesicles containing electron-dense proteinaceous material, normal appearance of basal membranes (Figures 7D–7I, asterisks), normal cell adhesion complexes with both apical junctional complexes (JCs) and gap junctions (GJs) (Figure 7Dii and 7Diii), and recognizable basal cells juxtaposed between baso-lateral domains of epithelial cells embraced by numerous telocytes (Figure 7Diii). In contrast, *Lgr5-DTR-EGFP* prostate tissues exhibited a significant disruption of the architectural organization, with the luminal cells having a reduced number of secretory vesicles and randomly intercalated basal cells (Figure 7Div and 7Dv). Adhesion to basal membranes was disrupted, with significant accumulation of electron-dense material in the intercellular space (Figure 7Dvi and 7Dvii, asterisks). Cell-cell interactions were also significantly

altered, exhibiting numerous filopodia-like projections (Figure 7Dvi, arrowheads) that did not establish recognizable adhesion complexes. These changes also reflect a response of the epithelial cells toward disturbed tissue homeostasis and are also consistent with the RNA-seq analysis showing a decreased Gene Ontology associated with the secretory function in the prostate epithelial cells (Figure 6B).

DISCUSSION

We show that ablating the Lgr5-expressing stromal cells impairs the ductal outlet control (Figures 7A and 7B) and causes a decreased prostate volume (Figure 3D) and increased cell density (Figure 3E) and tissue stiffness (Figure 7C). This alters cell-cell and cell-ECM interactions (Figure 7D) and activates the mechanosensory MAPK signaling (Figure 6C), presumably by augmenting the integrin signaling via interaction of the cells and ECM. We showed previously that the proximal stromal cells secrete transforming growth factor β (TGF-β) and Wnt ligands to suppress proliferation of the adjacent epithelial cells (Wei et al., 2019). Together, these studies reveal that the proximal prostatic stromal cells maintain prostate homeostasis via both paracrine signaling and structural support. Our study highlights that the anatomic location of the stromal cells can dictate their significance in maintaining tissue homeostasis. Cells in the tissues with high surface tension, such as lung alveolars, or near transitional areas where different organs meet, such as hilum and esophagogastric junction, are more likely to affect organ homeostasis in a relatively long-distance manner by leveraging the mechanotransduction signaling.

LGR5 is recently reported to be expressed by an abundant fibroblast subset in human skin tissues (Gur et al., 2022). Nevertheless, we did not find any stromal cells that express *LGR5* in human periurethral prostates by RNA *in situ* analysis (data not shown). However, the mouse $Lgr5^+$ stromal cells share molecular features with the human prostate interstitial stromal cells, which are also denser at the periurethral prostate (Joseph et al., 2021). These similarities suggest that they may mediate similar biological functions. Lgr5 is also expressed by the stromal cells in other mouse organs, such as the lung alveolar mesenchymal cells (Lee et al., 2017; Zepp et al., 2017) and intestinal villus tip telocytes (Bahar Halpern et al., 2020). These cells and the $Lgr5^+$ prostate stromal cells (Wei et al., 2019) all express abundant Wnt ligands such as Wnt3a, Wnt5b, etc., and regulate epithelial cell biology in a paracrine manner. They have been shown to regulate zonation of intestinal enterocyte genes, control self-renewal and differentiation of the lung club epithelial cells, and suppress proximal prostate epithelial cell proliferation, respectively. The unique anatomic distribution of the prostatic $Lgr5^+$ stromal cells and the low turnover rate of the prostate epithelia granted us the opportunity to reveal the previously un-appreciated nonparacrine role of the $Lgr5^+$ stromal cells in maintaining tissue integrity and homeostatic mechanoforce. In contrast, it was difficult to determine whether the $Lgr5^+$ stromal cells in the intestine and lung also mediate similar biology because of the fast cell turnover rate in the intestine and wide-spread distribution of the Lgr5-expressing stromal cells in the lung. Interestingly, genetic ablation of the $Lgr6^+$ mesenchymal cells (which overlap with some $Lgr5^+$ stromal cells) also induced acute and transient higher proliferation rate of airway epithelial cells (Lee et al., 2017), which could be at least partially resulted from the tissue-damage-associated alteration of mechanoforce.

We showed that the enhanced MAPK kinase activity is responsible for the increased epithelial proliferation upon ablation of the $Lgr5^+$ cells. However, the molecular mechanisms underlying the increased apoptosis and emergence of TACs remain unclear. We showed an increased apoptosis in prostate epithelial cells in the *Lgr5*-null mice, indicating that the stromal expression of *Lgr5* per se may regulate epithelial cell survival. Alternatively, we also showed that ablating the $Lgr5^+$ stromal cells caused cell crowding. Apoptosis could be a result of the crowding-induced cell extrusion and delamination (Eisenhoffer et al., 2012; Marinari et al., 2012). JUN N-terminal kinase (JNK) has been shown to play a pro-apoptotic role in cell competition (de la Cova et al., 2004). Consistently, we noticed an increased activity of JNK and its downstream effector c-Jun after ablation of the $Lgr5^+$ cells by immunostaining, although the observation cannot be substantiated by western blot. Basal-to-luminal differentiation and acquisition of a TAC phenotype are also frequently noted in the mouse models of prostate tissue damage (Kwon et al., 2014; Toivanen et al., 2016) and cancer (Choi et al., 2012). The underlying molecular mechanism remains unclear but is likely caused by the changes in cell-cell and cell-ECM interactions. Finally, the loss of sympathetic nerve upon ablation of the $Lgr5^+$ cells is also an intriguing observation. It has been shown that softer substrates accelerate the formation dynamics of oriented neuronal networks (Lantoine et al., 2016). Therefore, the loss of sympathetic nerve is probably a result of an increased tissue stiffness. This is also supported by our observation that the density of the sympathetic nerve also decreased in the prostate tissues of castrated mice, which are stiffer than those of intact mice. The other potential mechanism that cannot be excluded is that the loss of sympathetic nerve may result from the depletion of unique paracrine signaling due to loss of the $Lgr5^+$ stromal cells.

Our study implies that normal physiology-associated changes in mechanical forces, such as that caused by ejaculation, may have a transient, but repetitive, impact on prostate tissue homeostasis and epithelial turnover. Since increased cell turnover can influence the initiation of benign or malignant hyperplasia, sexual frequency may have an impact on the development of the prostate-related diseases. The correlation has been interrogated by some association studies using human subjects, but the conclusions were contradictory (Fernandez et al., 2005; Jacobsen et al., 2003; Leitzmann et al., 2004; Oishi et al., 1990; Rider et al., 2016) due to various confounding factors (Annweiler et al., 2017; Garcia-Perdomo and Manzano Nunez, 2016). Therefore, mouse models may be used in the future to determine the impact of physiology- or pathobiology-associated changes in mechanical signaling on the initiation and progression of benign and malignant diseases in the prostate.

Limitations of the study

In the prostate tissues of the *Lgr5-DTR-EGFP* and *Lgr5-EGFP-IRES-CreER^{T2}* models, the expression of EGFP is undetectable by immunostaining but is weakly detected by FACS. This posed some challenges to us while designing the lineage tracing and co-immunostaining studies but did not affect how we interpreted the results because EGFP is mostly restricted to the proximal prostatic ducts and is distinguishably weaker than the EYFP reporter by FACS.

The phenotypes that we observed in this study were mostly restricted to the AP. This is probably because the AP is more sensitive to the disruption of lumen integrity since it displays a more lobular structure, whereas the VP and DLP manifest a more homogeneous tubular structure. The lack of obvious phenotype in the DLP and VP also implies that eliminating the rare $Lgr5^+$ cells unlikely alters tissue homeostasis by depriving paracrine signaling. This is consistent with our data showing that nonselectively ablating a small percentage of stromal cells throughout the prostate using the *Col1a2-CreER^{T2}* model did not phenocopy ablation of the $Lgr5^+$ stromal cells. This observation implies that partial reduction of the paracrine signaling from prostate stromal cells is tolerable unless there is critical paracrine signaling uniquely from the $Lgr5^+$ stromal cells.

Finally, a previous study showed that very rare prostate epithelial cells express *Lgr5* (0.023% of total prostate cells) (Wang et al., 2015). The group ablated those cells using the same *Lgr5-DTR* model and concluded that those cells played a role in prostate tissue regeneration and were the putative prostate stem cells. In our study, we cannot confirm the existence of such cells by immunostaining but identified abundant $Lgr5^+$ stromal cells in the proximal ducts. Based on our results, we reasoned that the rapid reduction of the prostate size in the DT-treated *Lgr5-DTR* model is likely due to the ablation of the $Lgr5^+$ stromal cells. However, we cannot rule out the possibility that the phenotypes could also be partially caused by the loss of those rare epithelial cells.

STAR★METHODS

RESOURCE AVAILABILITY

Lead contact—Further information and requests for resources and reagents should be directed to and will be fulfilled by the lead contact, Li Xin (xin18@uw.edu).

Materials availability—No unique material was generated in this study. Experimental protocols developed in this study will be shared by the lead contact upon request.

Data and software availability

- The RNA-seq data of the FACS-isolated basal, luminal, and stromal cells in the anterior prostate of DT-treated *Lgr5-DTR-eGFP* and control mice in this paper were deposited to GEO (GSE190938).
- This paper does not report original code.
- Any additional information required to reanalyze the data reported in this paper is available from the lead contact upon request.

EXPERIMENTAL MODEL AND SUBJECT DETAILS

Mice—All animals used in this study received humane care in compliance with the principles stated in the Guide for the Care and Use of Laboratory Animals, NIH Publication, 1996 edition, and the protocol was approved by the Institutional Animal Care Committee of Universityof Washington. The C57BL/6 and SCID/Beige mice were purchased from Charles River (Wilmington, MA). *Lgr5-DTR-eGFP* mice were originally

generated by Genentech (Tian et al., 2011) and were kindly provided by Dr. Noah Shroyer at the Baylor College of Medicine. *Krt7-CreER^{T2}* was kindly provided by Dr. Jianwen Que at Columbia University. *Krt8-CreER^{T2}* was made by our laboratory as described (Zhang et al., 2012). C57BL/6-*Gt(ROSA)26Sor$^{tm1(HBEGF)Awai}$*/J, B6.Cg-*Gt(ROSA)26Sor$^{tm14(CAG-tdTomato)Hze}$*/J, *B6.129P2-Lgr5$^{tm1(cre/ERT2)Cle}$/J, Col1a2-CreER^{T2}*, *Pdgfrβ-CreER^{T2}*, *NG2-CreER^{T2}*, B6.Cg-*Gt(ROSA)26Sor$^{tm3(CAG-EYFP)Hze}$*/J mice were from the Jackson Laboratory (Bar Harbor, ME). Male mice at the age of E15.5 to postnatal 27 weeks were used. Mice were genotyped by polymerase chain reaction using mouse genomic DNA from tail biopsy specimens. The sequences of genotyping primers and the expected band sizes for PCR are listed in Table S3. PCR products were separated electrophoretically on 1% agarose gels and visualized via ethidium bromide under UV light.

METHOD DETAILS

Open-top light-sheet (OTLS) 3D microscopy—Prostate tissues from C57BL/6 mice were cleared and labeled by the anti-GFP antibody for eYFP staining following a modified iDISCO protocol (Renier et al., 2014) by using a milder index-matching reagent ethyl cinnamate. Cleared and labeled specimens were placed in custom 3D machined sample holders as described previously (Glaser et al., 2019). The samples were imaged on a Lightspeed Microscopy open-top light-sheet microscope with 20× magnification (0.44 microns per pixel) using a multi-immersion objective (#54–10–12, Special Optics, distributed by Applied Scientific Instrumentation). The fluorescence was filtered with band-pass filters for the 488 nm (for eYFP and EdU staining; FF03–525/50–25, Semrock) and 638 nm (for TOPRO3 nuclear staining; FF01–721/65–25, Semrock) excitation wavelengths. The raw image files were aligned and stitched in ImageJ using BigStitcher software (Hörl et al., 2019) and fused to TIFF files. The resulting TIFF files were visualized and analyzed using Aivia software (Aivia v8.5, DRVision Technologies LLC, Bellevue, WA). Aivia Pixel Classifier tool was used to segment and enumerate individual nuclei, eYFP and EdU signals.

RNA-Scope—Fresh tissues were collected and fixed by 10% neutral buffered formalin for 16–32 h at room temperature. Samples were embedded in paraffin blocks and cut into 5 μm sections for staining. Freshly cut slides were air-dried overnight at room temperature, then baked for 1 h at 60°C. The RNA-Scope *in situ* hybridization was performed by using RNA-Scope 2.5 HD Detection Reagent Red Kit (Advanced Cell Diagnostics, Newark, CA) following the manufacturer's standard protocol.

RNA isolation and quantitative RT–PCR—Total RNA was extracted using NucleoSpin RNA Plus XS Kit (Macherey-Nagel, Bethlehem, PA). RNA was reverse transcribed to cDNA using iScript™ Reverse Transcription Supermix for RT-qPCR (BioRad, Hercules, CA). QRT-PCR was performed using iTaq™ Universal SYBR Green Supermix (BioRad, Hercules, CA) and detected on a Quantstudio Real-Time PCR system (Applied Biosystems, Foster City, CA). The qPCR primer sequences for mouse *Lgr5* gene were CAACCTCAGCGTCTTCACCT (forward, 5' to 3') and AAGCAGAGGCGATGTAGGAG (reverse, 5' to 3').

Diphtheria toxin, tamoxifen, BrdU, EdU, 6-OHDA and trametinib treatment— Diphtheria toxin (D0564, Sigma-Aldrich, St. Louis, MO) (50ng/g/day) was dissolved in PBS and administrated i.p. into *Lgr5-DTR-eGFP* and control mice. Tamoxifen (Sigma-Aldrich, St. Louis, MO) was dissolved in corn oil and administrated i.p. into experimental mice at the specified age and dosage. BrdU (B5002–5G, Sigma-Aldrich, St. Louis, MO) (80 mg/kg/day) was administered one day before mice were sacrificed. EdU (900584–50MG, Sigma-Aldrich, St. Louis, MO) (10 mg/kg/day) was administered for 3 days before mice were sacrificed for 3D imaging. 6OHDA (H4381–500MG, Sigma-Aldrich, St. Louis, MO) was dissolved in sterile saline with 0.02% ascorbic acid and administrated to C57BL/6 male mice twice via intraperitoneal injection (100mg/kg at day 0 and 250mg/kg at day 2). Trametinib (S2673, Selleckchem.com) (1mg/kg) was administrated twice per day via oral gavage.

Flow cytometry and cell sorting—Dissociated mouse prostate single cells were incubated with florescence conjugated antibodies at 4°C for 30 minutes. Information for the antibodies for FACS analysis and sorting is listed in Key Resource Table. FACS analyses and sorting were performed using the BD LSR II and Aria III (BD Biosciences, San Jose, CA), respectively.

Histology and immunostaining—Prostate tissues were fixed by 10% buffered formalin and embedded in paraffin. H&E staining and immunofluorescence staining were performed using 5μm sections. For hematoxylin and eosin staining, sections were processed as described previously (Choi et al., 2012). For immunostaining, sections were processed as described previously (Choi et al., 2012) and incubated with primary antibodies in 3% normal goat serum (Vector Laboratories, Burlingame, CA) at 4°C overnight. Information for the antibodies is listed in Key Resource Table. Slides then were incubated with secondary antibodies labeled with fluorophores (diluted 1:250 in 3% normal goat serum). Sections were counterstained with NucBlue Fixed Cell ReadyProbes Reagent (DAPI) (Invitrogen, Waltham, MA). Immunofluorescence staining was imaged using a Nikon A1R confocal microscope (Nikon, NY, USA). Images of immunofluorescence staining were analyzed by Fiji ImageJ. Cell number was determined by using the count feature in the software.

Western blots—Cells were lysed in RIPA buffer (20 mM Tris-HCl, pH 7.5, 150 mM NaCl, 1 mM Na_2EDTA, 1 mM EGTA, 1% NP-40, 1% sodium deoxycholate, 2.5 mM sodium pyrophosphate, 1 mM b-glycerophosphate, 1 mM Na_3VO_4) with protease inhibitors and phosphatase inhibitors (Roche Applied Science, Indianapolis, IN). Protein concentrations were determined by the Quick Start™ Bradford 1x Dye Reagent (Bio-Rad, Hercules, CA). Proteins were separated by 10% SDS/PAGE and transferred onto a nitrocellulose membrane (Amersham Biosciences, Arlington Heights, IL). The membrane was blocked in 5% BSA, subsequently incubated with primary antibodies listed in Key resources table at 4°C overnight followed by incubation with peroxidase-conjugated goat anti-mouse IgG or goat anti-rabbit IgG (Vector Laboratories, Burlingame, CA), developed with Immobilon Classico Western HRP Substrate (Millipore, Burlington, MA) and imaged by Amersham Imager 600 (GE Healthcare, Chicago, IL).

Renal capsule implantation—Urogenital sinuses (UGS) were dissected from *Lgr5* null and control male embryos. The UGS tissues were implanted under the renal capsules of SCID/Beige male hosts as described previously (Valdez et al., 2012) with androgen pellets (15 mg/pellet, Sigma-Aldrich, St Louis, MO) placed subcutaneously.

Liquid chromatography triple quadruple mass spectrometry steroid analysis —Stable isotope labeled internal standard testosterone-2,3,4-$^{13}C_3$, were purchased from IsoSciences (King of Prussia, PA). Testosterone (T) pure standards was purchased from Steraloids (Newport, RI), and hydroxylamine hydrochloride, ultrapure methanol, and water (Chromasolv®) from SigmaAldrich (St. Louis, MO). Internal T-$^{13}C_3$ (0.5 ng) standard was added to mouse sera. An Agilent 6495 triple quadruple mass spectrometer (Agilent, Santa Clara, CA) equipped with a Jet Stream electrospray ion source (ESI, Agilent), a 1290 Infinity ultrahigh performance liquid chromatography system (Agilent) and MassHunter Workstation software (Agilent) was used to quantify testosterone in this study. Chromatographic separation of steroid oximes was conducted with a Chromolith C18 reverse phase column (50–2 mm) with a matching Chromolith guard column (5–2 mm). Testosterone oxime was introduced into ESI source and analyzed in the positive ion mode. Molecular ions for T (m/z 304.2) and for $^{13}C_3$ internal standard T (m/z 307.2) were selected in the first quadrupole and quantified using product ion for T (m/z 124.1) and for internal standard T (m/z 127.1). The lower limit of quantification on column for T was 2.5 fg.

LC-MS/MS analysis for mouse prostate fluids and urine samples—Individual mouse anterior prostates were collected and cut for 10 times using micro scissors in 1.5mL tubes and rinsed in 50μL PBS. After a brief spin down at 4°C, supernatant was collected and frozen at −80°C for downstream LC-MS/MS analysis. Proteins from mouse prostate fluids and urine samples were first diluted by SDS (the final concentration was 5%). After determining the protein concentration using Pierce™ BCA protein assay (Thermo Fisher Scientific, Waltham, MA), the proteins (50 mg) were denatured with 10 mM DTT for 15 min at 37°C and alkylated with 50 mM iodoacetamide in the dark for 15 min at room temperature. Afterward, the samples were added a final concentration of 2.5% phosphoric acid and then six volumes of “binding” buffer (90% methanol; 100 mM triethylammonium bicarbonate, TEAB; pH 7.1). After mixing, the protein solution was loaded to an S-Trap filter (Protifi, Huntington, NY), spun at 10,000 g for 1 min and then the filter was washed with 150 μL of binding buffer 3 times. Finally, 2 μg of Lys-C and sequencing-grade trypsin and 20 μL of digestion buffer (50 mM TEAB) were added into the filter and digested at 37°C for 16 h. To elute peptides, 40 μL of 50 mM TEAB, 40 μL of 0.2% formic acid in H_2O, and 40 μL of 50% acetonitrile in H_2O were added sequentially. The peptide solutions were pooled and quantified by BCA protein assay. The peptides were dried with SpeedVac and stored at −80°C until LC-MS/MS analysis.

Lyophilized peptides were reconstituted in 15 μL of 0.1% TFA with 2% ACN containing 0.01% DDM (Tsai et al., 2021) to reach a concentration of 0.1 μg/μL and 5 μL of the resulting sample was analyzed by LC-MS/MS using an Orbitrap Eclipse Tribrid Mass Spectrometer (Thermo Fisher Scientific, Waltham, MA) connected to a nanoACQUITY UPLC system (Waters, Milford, MA). Peptides were separated on an analytical column (75

μm i.d. × 20 cm) packed using 1.9-μm ReproSil C18 and with a column heater set at 48°C, using an LC gradient (buffer A: 0.1% FA with 3% ACN and buffer B: 0.1% FA in 90% ACN): 2–6% buffer B in 1 min, 6–30% buffer B in 84 min, 30–60% buffer B in 9 min, 60–90% buffer B in 1 min, and finally 90% buffer B for 5 min at 200 nL/min. Peptides were ionized by applying a voltage of 2,400 V with a FAIMS (high field asymmetric waveform ion mobility spectrometry) source. The ionized peptides were fractionated by the FAIMS Pro interface using a 3-CV (−45, −60 and −75 CV) method. Data were acquired in a data-dependent acquisition mode and the peptides were isolated using a quadrupole system (the isolation window was 0.7). Fractionated ions with a mass range 400–1800 m/z were scanned at 120,000 resolutions with automatic ion injection time (IT) and an 100% automatic gain control (AGC) target (4E5). Precursor ions with intensities > 1E4 were selected for fragmentation by higher-energy collisional dissociation (HCD) at 32% collision energy. The fragment ions were detected by the Orbitrap (resolution 5,000) The AGC target for MS/MS was 1.25E5 with automatic ion injection time (IT).

The raw MS/MS data were processed with MSFragger via FragPipe (Kong et al., 2017; Teo et al., 2021). The MS/MS spectra were searched against a Mus musculus (Mouse) UniProt database (fasta file dated July 31, 2021 with 34,386 sequences which contain 17,193 decoys) and (initial) fragment mass tolerances were set to 20 ppm. A peptide search was performed with full tryptic digestion (Trypsin) and allowed a maximum of two missed cleavages. Carbamidomethyl (C) was set as a fixed modification; acetylation (protein N-term) and oxidation (M) were set as variable modifications. For match-between-run (MBR) analysis, 10 ppm m/z tolerance, 1.5-min retention time (RT) tolerance and 0.05 MBR ions FDR were used for analysis. The final reports were then generated (peptide-spectrum match (PSM), ion, peptide, and protein) and filtered at each level (1% protein FDR plus 1% PSM/ion/peptide-level FDR). The MaxLFQ_intensity of each protein were extracted from FragPipe outputs (combined protein.tsv) and analyzed by Perseus (Tyanova et al., 2016) for statistical analyses. For the volcano plot analysis, the intensity of overlapping proteins from 4 groups were transformed to log2 scale. The quantifiable protein was defined as a protein having signal intensities in at least 3 valid values in one sample group. Missing values were imputed from normal distribution with a width of 0.3 and a down shift of 1.8. T test ($p < 0.05$) was applied to determine the significantly expressed proteins.

Atomic force microscopy—An Asylum Research Cypher AFM was used for force curve measurement with an MLCT silicon nitride multi probe chip (Bruker, Billerica, MA). Probe E was used for all measurements with a nominal spring constant of 0.1 N/m and 38 kHz frequency. All other probes were removed prior to use. The actual spring constant was calculated by measuring the sensitivity on a quartz substrate and the resonant frequency by thermal tuning the cantilever. The probe and sample were submerged in DMEM medium with 1% Pluronic F127. The Pluronic solution acts as a surfactant and prevents excessive adhesion of the probe and sample. All force curves were performed at 500nm/s. Force curves were fit using a Hertzian model during the tip extension part of the curve to extract the elastic modulus. All fits were performed using the Asylum Research force curve analysis software. Poor curves were removed before calculating the average and standard deviation of the samples.

Electron microscopy—Transcardial perfusion was performed to fix mouse tissues using paraformaldehyde/glutaraldehyde perfusant [2% paraformaldehyde (Ted Pella Inc., Redding, CA) + 2.5% glutaraldehyde (Ted Pella Inc., Redding, CA) + 2mM $CaCl_2$ in 0.1M sodium cacodylate (Ted Pella Inc., Redding, CA), pH = 7.4]. Prostate tissues were dissected after perfusion and processed for electron microscopic analysis. Samples were stained with saturated uranyl acetate and Reynold's lead citrate and reviewed using a Hitachi H7500 transmission electron microscope.

RNA-seq—NucleoSpin RNA XS Kit (Macherey-Nagel, Bethlehem, PA) was used to purify RNAs from FACS-isolated mouse prostate basal, luminal and stromal cells. Reverse transcriptions were performed using SMART-Seq™ v4 Ultra™ Low Input RNA Kit for Sequencing (Clontech Laboratories, Mountain View, CA). CDNA libraries were prepared using a Nextera XT DNA Library Preparation Kit (Illumina, San Diego, CA), and were sequenced using a HiSeq 2500 sequencer. Sequenced reads in FASTQ files were mapped to mm10 whole genome using Tophat2, and Fragments Per Kilobase of transcript per Million mapped reads (FPKM) were calculated using Cufflinks. Genes found differentially expressed ($p < 0.05$ by t test, and minimum 1.4-fold change) were evaluated for enrichment of Gene Ontology (GO) gene classes, using SigTerms software (Creighton et al., 2008). Data have been deposited at GEO.

QUANTIFICATION AND STATISTICAL ANALYSIS

All experiments were performed using at least 3 mice in independent experiments. Data are presented as means ± SD. Student's t test was used to determine the significance in two-group experiments. One-way ANOVA test was used to determine the significance in multiple-group experiments. For all statistical tests, the two-tail $p \leq 0.05$ level of confidence was accepted for statistical significance.

Supplementary Material

Refer to Web version on PubMed Central for supplementary material.

ACKNOWLEDGMENTS

This work was supported by R01DK092202 and R01DK107436 (L.X.), the Pritt Family endowment, and the Institute for Prostate Cancer Research (IPCR).

REFERENCES

Annweiler C, Bigot P, Karras SN, Rider R:JR, Wilson KM, Sinnott JA, Kelly RS, Muccia LA, and Edward L (2017). Giovannucci. Ejaculation frequency and risk of prostate cancer: updated results with an additional decade of follow-up. Eur. Urol 70, 974–982.

Aragona M, Sifrim A, Malfait M, Song Y, Van Herck J, Dekoninck S, Gargouri S, Lapouge G, Swedlund B, Dubois C, et al. (2020). Mechanisms of stretch-mediated skin expansion at single-cell resolution. Nature 584, 268–273. [PubMed: 32728211]

Ayala GE, Wheeler TM, Shine HD, Schmelz M, Frolov A, Chakraborty S, and Rowley D (2001). In vitro dorsal root ganglia and human prostate cell line interaction: redefining perineural invasion in prostate cancer. Prostate 49, 213–223. [PubMed: 11746267]

Bahar Halpern K, Massalha H, Zwick RK, Moor AE, Castillo-Azofeifa D, Rozenberg M, Farack L, Egozi A, Miller DR, Averbukh I, et al. (2020). Lgr5+ telocytes are a signaling source at the intestinal villus tip. Nat. Commun 11, 1936. [PubMed: 32321913]

Barker N, van Es JH, Kuipers J, Kujala P, van den Born M, Cozijnsen M, Haegebarth A, Korving J, Begthel H, Peters PJ, and Clevers H (2007). Identification of stem cells in small intestine and colon by marker gene Lgr5. Nature 449, 1003–1007. [PubMed: 17934449]

Chen CS (2008). Mechanotransduction - a field pulling together? J. Cell Sci 121, 3285–3292. [PubMed: 18843115]

Choi N, Zhang B, Zhang L, Ittmann M, and Xin L (2012). Adult murine prostate basal and luminal cells are self-sustained lineages that can both serve as targets for prostate cancer initiation. Cancer Cell 21, 253–265. [PubMed: 22340597]

Creighton CJ, Nagaraja AK, Hanash SM, Matzuk MM, and Gunaratne PH (2008). A bioinformatics tool for linking gene expression profiling results with public databases of microRNA target predictions. RNA 14, 2290–2296. [PubMed: 18812437]

de la Cova C, Abril M, Bellosta P, Gallant P, and Johnston LA (2004). Drosophila myc regulates organ size by inducing cell competition. Cell 117, 107–116. [PubMed: 15066286]

Eisenhoffer GT, Loftus PD, Yoshigi M, Otsuna H, Chien CB, Morcos PA, and Rosenblatt J (2012). Crowding induces live cell extrusion to maintain homeostatic cell numbers in epithelia. Nature 484, 546–549. [PubMed: 22504183]

Engler AJ, Sen S, Sweeney HL, and Discher DE (2006). Matrix elasticity directs stem cell lineage specification. Cell 126, 677–689. [PubMed: 16923388]

Fernández L, Galán Y, Jiménez R, Gutiérrez A, Guerra M, Pereda C, Alonso C, Riboli E, Agudo A, and González C (2005). Sexual behaviour, history of sexually transmitted diseases, and the risk of prostate cancer: a case-control study in Cuba. Int. J. Epidemiol 34, 193–197. [PubMed: 15375086]

Garcia-Perdomo HA, Manzano Nunez R, Rider RJR, Wilson KM, Sinnott JM, Kelly RS, and Mucci LA (2016). Edward L. Giovannucci. Ejaculation frequency and risk of prostate cancer: updated results with an additional decade of follow-up. Eur urol 70, e155. [PubMed: 27156130]

Glaser AK, Reder NP, Chen Y, Yin C, Wei L, Kang S, Barner LA, Xie W, McCarty EF, Mao C, et al. (2019). Multi-immersion open-top light-sheet microscope for high-throughput imaging of cleared tissues. Nat. Commun 10, 2781. [PubMed: 31273194]

Gur C, Wang SY, Sheban F, Zada M, Li B, Kharouf F, Peleg H, Aamar S, Yalin A, Kirschenbaum D, et al. (2022). LGR5 expressing skin fibroblasts define a major cellular hub perturbed in scleroderma. Cell 185, 1373–1388.e20. [PubMed: 35381199]

Hörl D, Rojas Rusak F, Preusser F, Tillberg P, Randel N, Chhetri RK, Cardona A, Keller PJ, Harz H, Leonhardt H, et al. (2019). BigStitcher: re-constructing high-resolution image datasets of cleared and expanded samples. Nat. Methods 16, 870–874. [PubMed: 31384047]

Ittmann M (2018). Anatomy and histology of the human and murine prostate. Cold Spring Harb. Perspect. Med 8, a030346. [PubMed: 29038334]

Jacobsen SJ, Jacobson DJ, Rohe DE, Girman CJ, Roberts RO, and Lieber MM (2003). Frequency of sexual activity and prostatic health: fact or fairy tale? Urology 61, 348–353. [PubMed: 12597946]

Jiang M, Li H, Zhang Y, Yang Y, Lu R, Liu K, Lin S, Lan X, Wang H, Wu H, et al. (2017). Transitional basal cells at the squamous-columnar junction generate Barrett's oesophagus. Nature 550, 529–533. [PubMed: 29019984]

Joseph DB, Henry GH, Malewska A, Reese JC, Mauck RJ, Gahan JC, Hutchinson RC, Malladi VS, Roehrborn CG, Vezina CM, and Strand DW (2021). Single-cell analysis of mouse and human prostate reveals novel fibroblasts with specialized distribution and microenvironment interactions. J. Pathol 255, 141–154. [PubMed: 34173975]

Kai F, Drain AP, and Weaver VM (2019). The extracellular matrix modulates the metastatic journey. Dev. Cell 49, 332–346. [PubMed: 31063753]

Kong AT, Leprevost FV, Avtonomov DM, Mellacheruvu D, and Nesvizhskii AI (2017). MSFragger: ultrafast and comprehensive peptide identification in mass spectrometry-based proteomics. Nat. Methods 14, 513–520. [PubMed: 28394336]

Kwon OJ, Choi JM, Zhang L, Jia D, Li Z, Zhang Y, Jung SY, Creighton CJ, and Xin L (2020). The Sca-1(+) and Sca-1(−) mouse prostatic luminal cell lineages are independently sustained. Stem Cell. 38, 1479–1491.

Kwon OJ, Zhang L, and Xin L (2016). Stem cell antigen-1 identifies a distinct androgen-independent murine prostatic luminal cell lineage with bipo-tent potential. Stem Cell. 34, 191–202.

Kwon OJ, Zhang L, Ittmann MM, and Xin L (2014). Prostatic inflammation enhances basal-to-luminal differentiation and accelerates initiation of prostate cancer with a basal cell origin. Proc. Natl. Acad. Sci. USA 111, E592–E600. [PubMed: 24367088]

Kwon OJ, Zhang Y, Li Y, Wei X, Zhang L, Chen R, Creighton CJ, and Xin L (2019). Functional heterogeneity of mouse prostate stromal cells revealed by single-cell RNA-seq. iScience 13, 328–338. [PubMed: 30878879]

Lantoine J, Grevesse T, Villers A, Delhaye G, Mestdagh C, Versaevel M, Mohammed D, Bruyère C, Alaimo L, Lacour SP, et al. (2016). Matrix stiffness modulates formation and activity of neuronal networks of controlled architectures. Biomaterials 89, 14–24. [PubMed: 26946402]

Lee JH, Tammela T, Hofree M, Choi J, Marjanovic ND, Han S, Canner D, Wu K, Paschini M, Bhang DH, et al. (2017). Anatomically and functionally distinct lung mesenchymal populations marked by Lgr5 and Lgr6. Cell 170, 1149–1163.e12. [PubMed: 28886383]

Leitzmann MF, Platz EA, Stampfer MJ, Willett WC, and Giovannucci E (2004). Ejaculation frequency and subsequent risk of prostate cancer. JAMA 291, 1578–1586. [PubMed: 15069045]

Marinari E, Mehonic A, Curran S, Gale J, Duke T, and Baum B (2012). Live-cell delamination counterbalances epithelial growth to limit tissue over-crowding. Nature 484, 542–545. [PubMed: 22504180]

McAuley E, Moline D, VanOpstall C, Lamperis S, Brown R, and Vander Griend DJ (2019). Sox2 expression marks castration-resistant progenitor cells in the adult murine prostate. Stem Cell. 37, 690–700.

Oishi K, Okada K, Yoshida O, Yamabe H, Ohno Y, Hayes RB, Schroeder FH, and Boyle P (1990). A case-control study of prostatic cancer in Kyoto, Japan: sexual risk factors. Prostate 17, 269–279. [PubMed: 2251222]

Peng YC, Levine CM, Zahid S, Wilson EL, and Joyner AL (2013). Sonic hedgehog signals to multiple prostate stromal stem cells that replenish distinct stromal subtypes during regeneration. Proc. Natl. Acad. Sci. USA 110, 20611–20616. [PubMed: 24218555]

Reder NP, Glaser AK, McCarty EF, Chen Y, True LD, and Liu JTC (2019). Open-top light-sheet microscopy image atlas of prostate core needle biopsies. Arch. Pathol. Lab Med 143, 1069–1075. [PubMed: 30892067]

Renier N, Wu Z, Simon DJ, Yang J, Ariel P, and Tessier-Lavigne M (2014). iDISCO: a simple, rapid method to immunolabel large tissue samples for volume imaging. Cell 159, 896–910. [PubMed: 25417164]

Rider JR, Wilson KM, Sinnott JA, Kelly RS, Mucci LA, and Giovannucci EL (2016). Ejaculation frequency and risk of prostate cancer: updated results with an additional decade of follow-up. Eur. Urol 70, 974–982. [PubMed: 27033442]

Rodriguez-Nieves JA, and Macoska JA (2013). Prostatic fibrosis, lower urinary tract symptoms, and BPH. Nat. Rev. Urol 10, 546–550. [PubMed: 23857178]

Sackmann-Sala L, Chiche A, Mosquera-Garrote N, Boutillon F, Cordier C, Pourmir I, Pascual-Mathey L, Kessal K, Pigat N, Camparo P, and Goffin V (2014). Prolactin-induced prostate tumorigenesis links sustained Stat5 signaling with the amplification of basal/stem cells and emergence of putative luminal progenitors. Am. J. Pathol 184, 3105–3119. [PubMed: 25193592]

Teo GC, Polasky DA, Yu F, and Nesvizhskii AI (2021). Fast deisotoping algorithm and its implementation in the MSFragger search engine. J. Proteome Res 20, 498–505. [PubMed: 33332123]

Tian H, Biehs B, Warming S, Leong KG, Rangell L, Klein OD, and de Sauvage FJ (2011). A reserve stem cell population in small intestine renders Lgr5-positive cells dispensable. Nature 478, 255–259. [PubMed: 21927002]

Toivanen R, Mohan A, and Shen MM (2016). Basal progenitors contribute to repair of the prostate epithelium following induced luminal anoikis. Stem Cell Rep. 6, 660–667.

Tsai CF, Zhang P, Scholten D, Martin K, Wang YT, Zhao R, Chrisler WB, Patel DB, Dou M, Jia Y, et al. (2021). Surfactant-assisted one-pot sample preparation for label-free single-cell proteomics. Commun. Biol 4, 265. [PubMed: 33649493]

Tsujimura A, Koikawa Y, Salm S, Takao T, Coetzee S, Moscatelli D, Shapiro E, Lepor H, Sun TT, and Wilson EL (2002). Proximal location of mouse prostate epithelial stem cells: a model of prostatic homeostasis. J. Cell Biol 157, 1257–1265. [PubMed: 12082083]

Tyanova S, Temu T, Sinitcyn P, Carlson A, Hein MY, Geiger T, Mann M, and Cox J (2016). The Perseus computational platform for comprehensive analysis of (prote)omics data. Nat. Methods 13, 731–740. [PubMed: 27348712]

Valdez JM, Zhang L, Su Q, Dakhova O, Zhang Y, Shahi P, Spencer DM, Creighton CJ, Ittmann MM, and Xin L (2012). Notch and TGFbeta form a reciprocal positive regulatory loop that suppresses murine prostate basal stem/progenitor cell activity. Cell Stem Cell 11, 676–688. [PubMed: 23122291]

Vining KH, and Mooney DJ (2017). Mechanical forces direct stem cell behaviour in development and regeneration. Nat. Rev. Mol. Cell Biol 18, 728–742. [PubMed: 29115301]

Wang BE, Wang X, Long JE, Eastham-Anderson J, Firestein R, and Junttila MR (2015). Castration-resistant Lgr5(+) cells are long-lived stem cells required for prostatic regeneration. Stem Cell Rep. 4, 768–779.

Wei X, Zhang L, Zhou Z, Kwon OJ, Zhang Y, Nguyen H, Dumpit R, True L, Nelson P, Dong B, et al. (2019). Spatially restricted stromal Wnt signaling restrains prostate epithelial progenitor growth through direct and indirect mechanisms. Cell Stem Cell 24, 753–768.e6. [PubMed: 30982770]

Wu H, Yu Y, Huang H, Hu Y, Fu S, Wang Z, Shi M, Zhao X, Yuan J, Li J, et al. (2020). Progressive pulmonary fibrosis is caused by elevated mechanical tension on alveolar stem cells. Cell 180, 107–121.e17. [PubMed: 31866069]

Zaichick V, and Zaichick S (2014). Age-related histological and zinc content changes in adult nonhyperplastic prostate glands. Age (Dordr) 36, 167–181. [PubMed: 23852618]

Zepp JA, Zacharias WJ, Frank DB, Cavanaugh CA, Zhou S, Morley MP, and Morrisey EE (2017). Distinct mesenchymal lineages and niches promote epithelial self-renewal and myofibrogenesis in the lung. Cell 170, 1134–1148.e10. [PubMed: 28886382]

Zhang L, Zhang B, Han S, Shore AN, Rosen JM, DeMayo FJ, and Xin L (2012). Targeting CreER(T2) expression to keratin 8-expressing murine simple epithelia using bacterial artificial chromosome transgenesis. Transgenic Res 21.

Highlights

- Stromal cells at the junction of mouse prostate and urethra highly express Lgr5
- Ablating $Lgr5^+$ stromal cells impairs the control of prostatic ductal outlet
- Ablating $Lgr5^+$ stromal cells activates a mechanosensory response
- Ablating $Lgr5^+$ stromal cells induces epithelial turnover and dedifferentiation

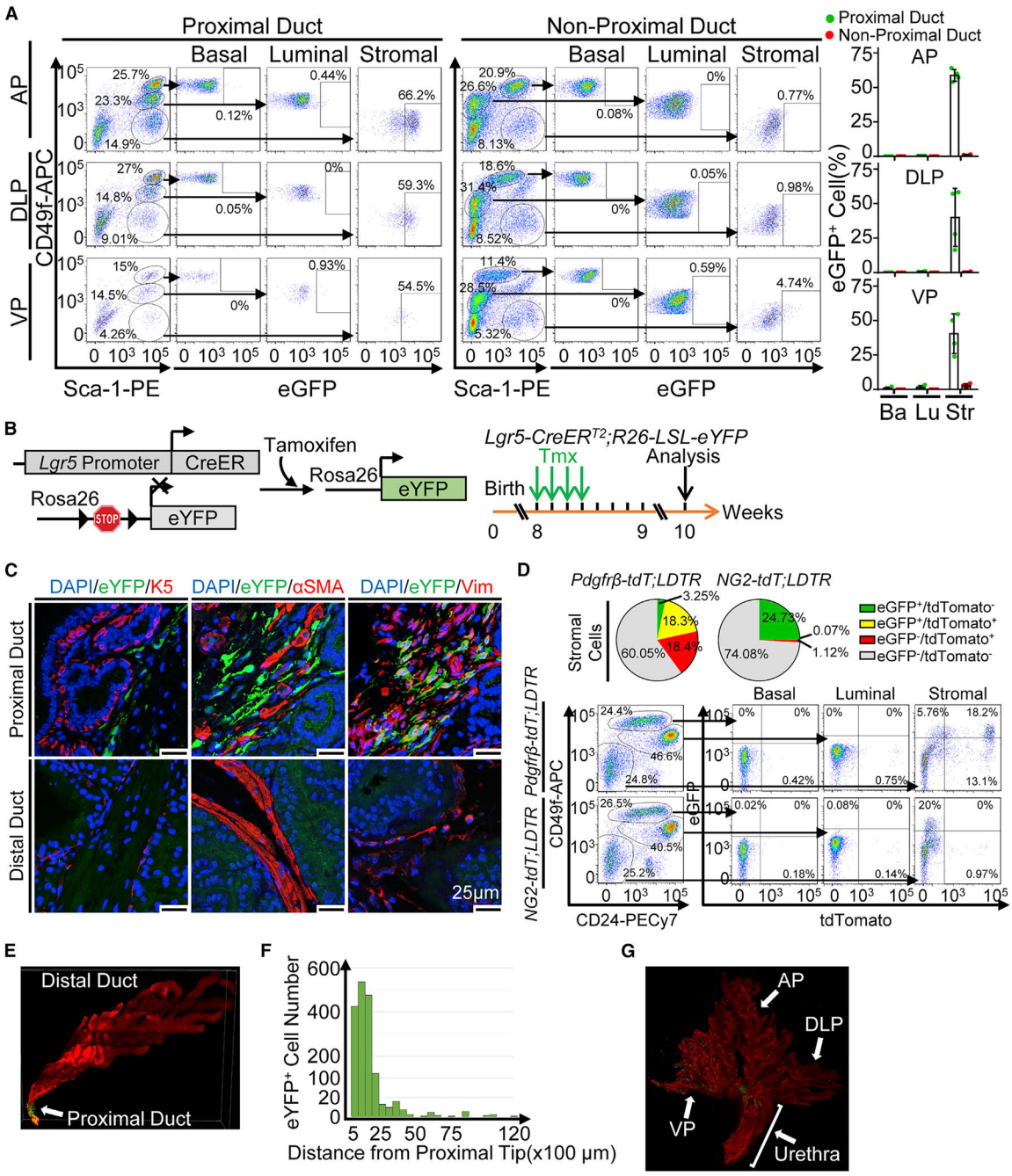

Figure 1. Lgr5^{+} stromal cells are localized at the proximal ducts of mouse prostate

(A) FACS plots of EGFP^{+} cells in Lin^{-}CD49f^{+}Sca-1^{+} basal cells, Lin^{-}CD49f^{-}Sca-1^{+} stromal cells, Lin^{-}CD49f^{Low}Sca-1^{-} distal (nonproximal) luminal cells, and Lin^{-}CD49f^{Low}Sca-1^{+} proximal luminal cells of anterior (AP), dorsolateral (DLP), and ventral (VP) prostate lobes of 10-week-old adult *Lgr5-DTR-EGFP* mice. Dot graphs show means ± SD of the percentage of EGFP^{+} cells in basal (Ba), luminal (Lu), and stromal (Str) cells of each prostatic lobe from 4 independent experiments.

(B) Schematic illustration of *Lgr5-CreER^{T2};R26-LSL-EYFP* (*Lgr5-EYFP*) mouse model and experimental design. Tmx, tamoxifen (5 mg/40 kg/day).
(C) Co-immunostaining of EYFP/Krt5, EYFP/αSMA and EYFP/Vimentin in proximal and distal ducts of the AP of 10-week-old *Lgr5-EYFP* mice after tamoxifen treatment. Scale bars, 25 μm.
(D) FACS plots of EGFP$^+$ and tdTomato$^+$ cells in Lin$^-$CD49f$^+$CD24^{Low} basal cells, Lin$^-$CD49f^{Low}CD24$^+$ luminal cells, and Lin$^-$CD49f$^-$CD24$^-$ stromal cells in the proximal APs of 10-week-old *Pdgfrβ-CreER^{T2};R26-LSL-tdTomato;Lgr5-DTR-EGFP* (*Pdgfrβ-tdT;LDTR*) and *NG2-CreER^{T2};R26-LSL-tdTomato;Lgr5-DTR-EGFP* (*NG2-tdT;LDTR*) mice. Pie graphs show percentage of EGFP$^+$/tdTomato$^-$ (green), EGFP$^+$/tdTomato$^+$ (yellow), EGFP$^-$/tdTomato$^+$ (red), and EGFP$^-$/tdTomato$^-$ (grey) stromal cells.
(E) Representative image of OTLS three-dimensional (3D) microcopy of EYFP$^+$ Lgr5-expressing cells in the AP of 10-week-old *Lgr5-EYFP* mice after tamoxifen treatment. Green: EYFP; red: TO-PRO-3 nuclear staining.
(F) Quantification of EYFP$^+$ Lgr5-expressing cell number along proximal-distal axis of AP lobe in OTLS 3D microcopy.
(G) Representative image of OTLS 3D microcopy of EYFP$^+$ Lgr5-expressing cells in the prostate and urethra of 10-week-old *Lgr5-EYFP* mice after tamoxifen treatment. Green: EYFP; red: TO-PRO-3 nuclear staining.

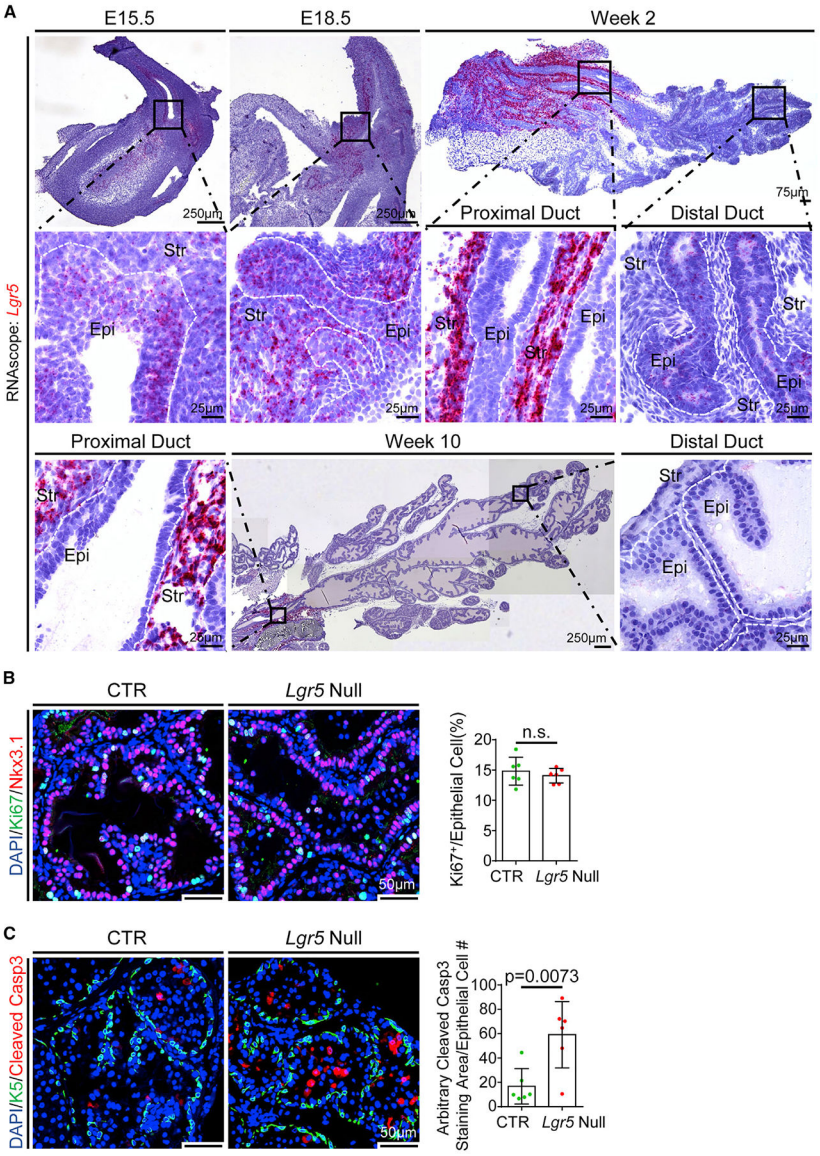

Figure 2. Lgr5 is dynamically expressed in the prostate and is dispensable for the prostate development

(A) RNA *in situ* analysis of *Lgr5* in E15.5 and E18.5 UGS and AP of 2- and 10-week-old C57BL/6 mice. Epi, epithelia; Str, stroma.

(B) Co-immunostaining of Ki67/Nkx3.1 in xenografts of *Lgr5*-null and control UGS. Scale bars, 50 μm. Dot graphs show means ± SD of the percentage of $Ki67^+$ cells in Nkx3.1-expressing prostatic epithelial cells. Each dot represents the result from one xenograft.

(C) Co-immunostaining of Krt5/cleaved caspase 3 (cleaved casp 3) in xenografts of *Lgr5*-null and control UGS. Scale bars, 50 μm. Dot graphs show means ± SD of cleaved casp 3 staining area normalized by prostatic epithelial cell number. Each dot represents result from one xenograft.

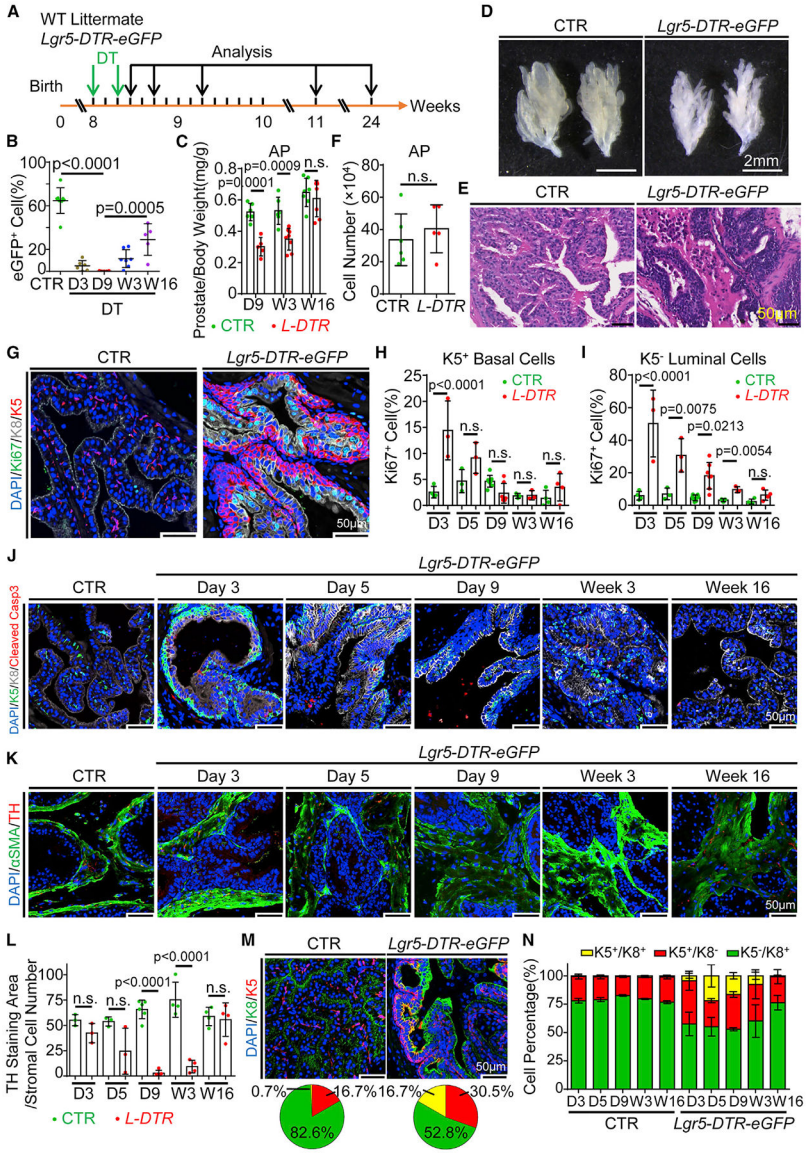

Figure 3. Ablating Lgr5^{+} stromal cells disrupts prostate homeostasis

(A) Schematic illustration of experimental design.

(B) Dot graphs show means ± SD of percentage of EGFP^{+} cells in Lin^{-}CD49f^{-}Sca-1^{+} proximal prostatic stromal cells of *Lgr5-DTR-EGFP* mice at day 3, day 9, week 3, and week 16 after treatment with diphtheria toxin (DT). Each dot represents the result from one mouse.

(C) Dot graphs show means ± SD of AP weight normalized by body weight at day 9, week 3, and week 16 after DT treatment. Each dot represents the result from one mouse.

(D) Transillumination images of the AP of *Lgr5-DTR-EGFP* and control mice at day 9 after DT treatment. Scale bars, 2 mm.

(E) H&E staining of the AP of DT-treated *Lgr5-DTR-EGFP* and control mice at day 9 after DT treatment. Scale bars, 50 μm.

(F) Dot graphs show means ± SD of total cell number of the AP of *Lgr5-DTR-EGFP* and control mice at day 9 after DT treatment. Each dot represents the result from one mouse.
(G) Co-immunostaining of Ki67/Krt8/Krt5 in the AP of *Lgr5-DTR-EGFP* and control mice at day 3 after DT treatment. Scale bars, 50 μm.
(H and I) Dot graphs show means ± SD of percentage of $Ki67^+$ cells in $Krt5^+$ prostatic basal cells (H) and $Krt5^-$ prostatic luminal cells (I) of the AP of *Lgr5-DTR-EGFP* and control mice at day 3, day 5, day 9, week 3, and week 16 after DT treatment. Each dot represents the result from one mouse.
(J) Co-immunostaining of Krt5/Krt8/cleaved casp 3 in the AP of *Lgr5-DTR-EGFP* and control mice at day 3, day 5, day 9, week 3, and week 16 after DT treatment. Scale bars, 50 μm.
(K) Co-immunostaining of αSMA/TH (tyrosine hydroxylase) in the AP of *Lgr5-DTR-EGFP* and control mice at day 3, day 5, day 9, week 3, and week 16 after DT treatment. Scale bars, 50μm.
(L) Dot graphs show means ± SD of TH staining area normalized by prostatic stromal cell number in the AP of *Lgr5-DTR-EGFP* and control mice at day 3, day 5, day 9, week 3, and week 16 after DT treatment. Each dot represents result from one mouse.
(M) Co-immunostaining of Krt8/Krt5 in the AP of *Lgr5-DTR-EGFP* and control mice at day 9 after DT treatment. Scale bars, 50μm. Pie graphs show percentage of $Krt5^+/Krt8^-$ (red), $Krt5^+/Krt8^+$ (yellow) and $Krt5^-/Krt8^+$ (green) epithelial cells.
(N) Bar graphs show percentage of $Krt5^+/Krt8^-$ (red), $Krt5^+/Krt8^+$ (yellow) and $Krt5^-/Krt8^+$ (green) epithelial cells in the AP of *Lgr5-DTR-EGFP* and control mice at day 3, day 5, day 9, week 3, and week 16 after DT treatment.

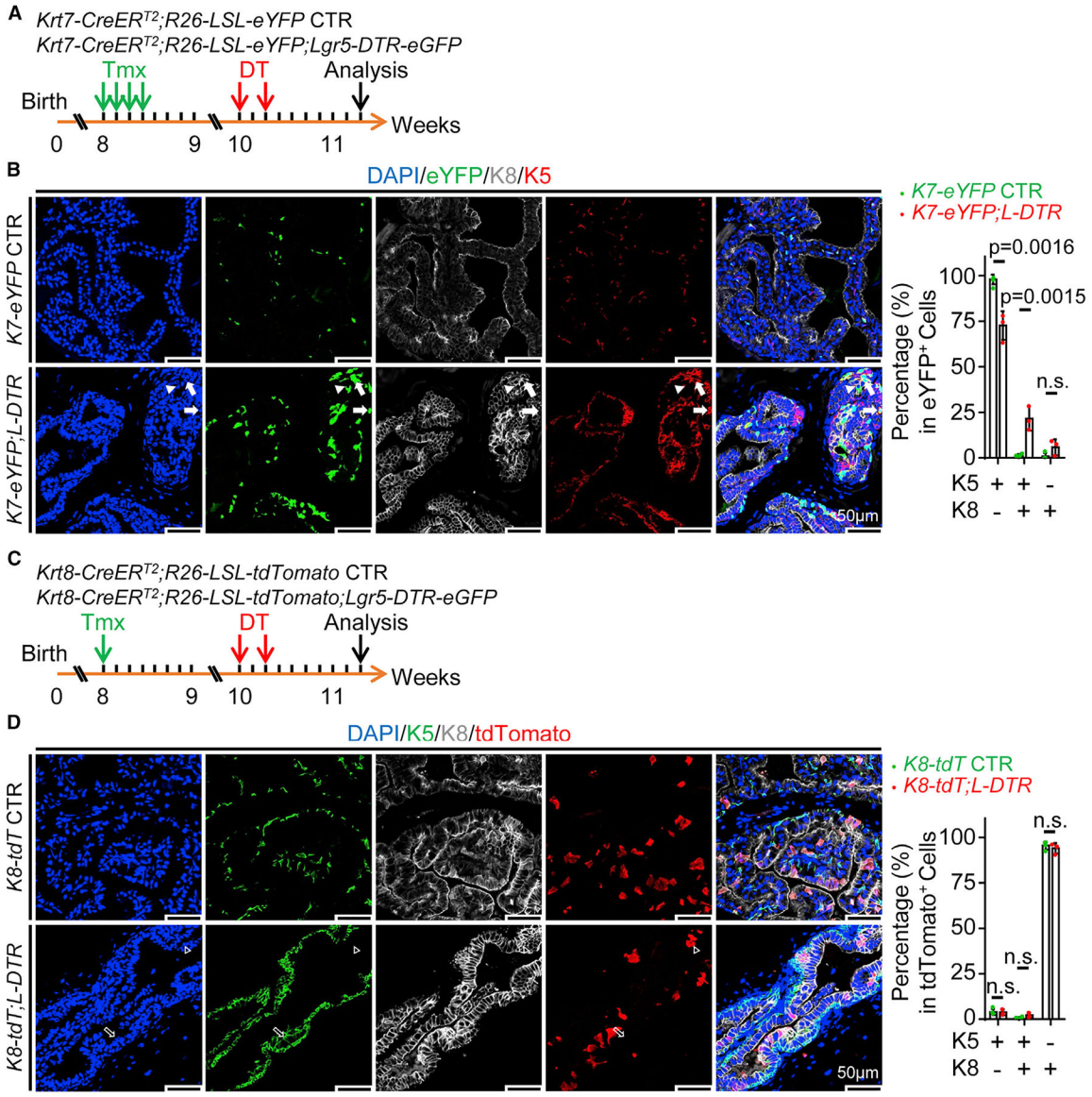

Figure 4. The Krt5$^+$/Krt8$^+$ transit-amplifying cells (TACs) are mainly derived from the basal cells

(A) Schematic illustration of experimental design of *Krt7-CreER^{T2};R26-LSL-eYFP;Lgr5-DTR-eGFP* (*K7-eYFP;L-DTR*) and control mice. Tmx: tamoxifen (2mg/40g/day).

(B) Co-immunostaining of eYFP/Krt8/Krt5 in the AP of *K7-eYFP;L-DTR* and *K7-eYFP* control mice at day 9 after DT treatment. Scale bars, 50μm. Arrows show Krt5$^+$/Krt8$^+$/eYFP$^+$ TACs. Arrowheads show Krt5$^-$/Krt8$^+$/eYFP$^+$ cells. Dot graphs show means ± SD of percentage of Krt5$^+$/Krt8$^-$, Krt5$^+$/Krt8$^+$ and Krt5$^-$/Krt8$^+$ epithelial cells in eYFP$^+$ cells in the AP of *K7-eYFP;L-DTR* and *K7-eYFP* control mice. Each dot represents result from one mouse.

(C) Schematic illustration of experimental design of *Krt8-CreER^{T2};R26-LSL-tdTomato;Lgr5-DTR-eGFP* (*K8-tdT;L-DTR*) and control mice. Tmx: tamoxifen (2mg/40g/day).

(D) Co-immunostaining of Krt5/Krt8/tdTomato in the AP of *K8-tdT;L-DTR* and *K8-tdT* control mice at day 9 after DT treatment. Scale bars, 50μm. Hollow arrows show $Krt5^{+}$/$Krt8^{+}$/$tdTomato^{-}$ TACs. Hollow arrowheads show $Krt5^{-}$/$Krt8^{+}$/$tdTomato^{+}$ cells. Dot graphs show means ± SD of percentage of $Krt5^{+}$/$Krt8^{-}$, $Krt5^{+}$/$Krt8^{+}$ and $Krt5^{-}$/$Krt8^{+}$ epithelial cells in the $tdTomato^{+}$ cells in the AP of *K8-tdT;L-DTR* and *K8-tdT* control mice. Each dot represents result from one mouse.

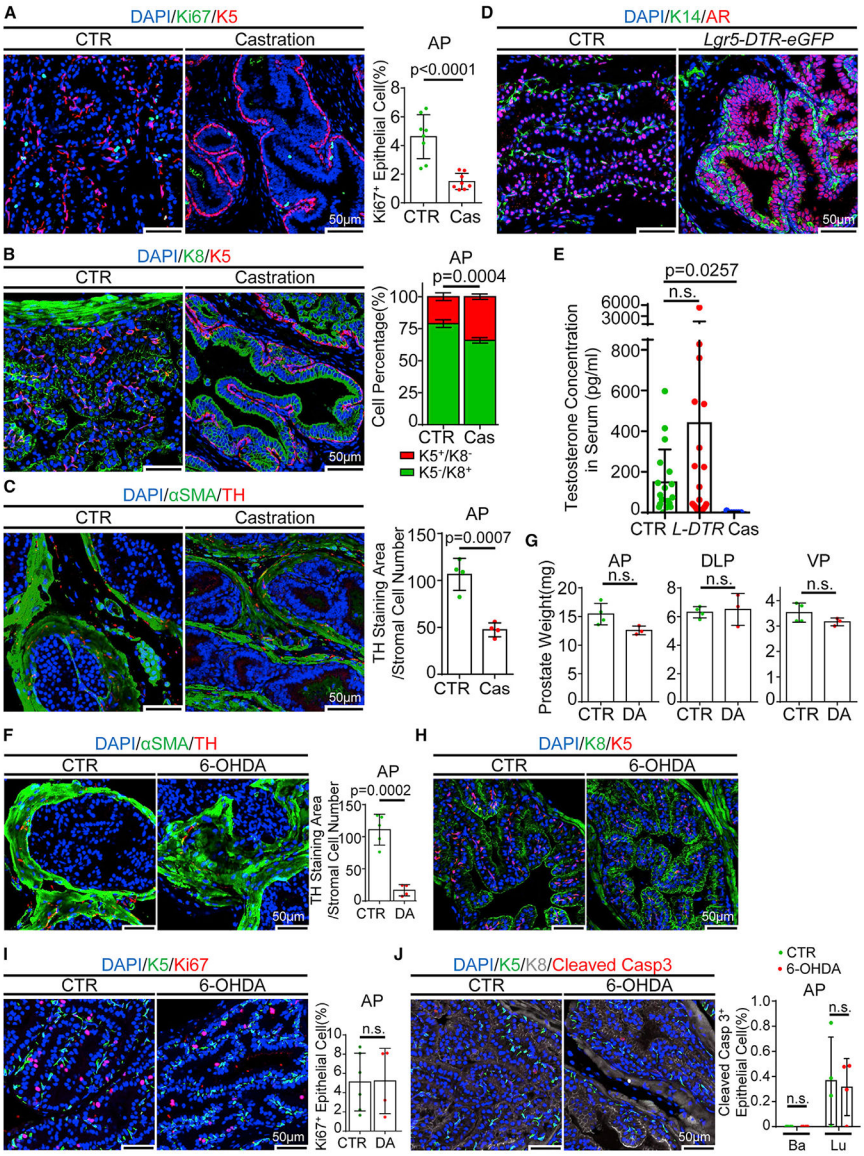

Figure 5. Ablating Lgr5^{+} stromal cells does not disrupt prostate homeostasis via endocrine or sympathetic nervous system

(A) Co-immunostaining of Ki67/Krt5 in the AP of castrated and control adult C57BL/6 mice. Scale bars, 50μm. Dot graphs show means ± SD of percentage of Ki67^{+} epithelial cells. Each dot represents result from one mouse.

(B) Co-immunostaining of Krt8/Krt5 in the AP of castrated and control adult C57BL/6 mice. Scale bars, 50μm. Bar graphs show means ± SD of percentage of Krt5^{+}/Krt8^{-} and Krt5^{-}/Krt8^{+} epithelial cells.

(C) Co-immunostaining of α-smooth muscle actin (αSMA)/TH in the AP of castrated and control adult C57BL/6 mice. Scale bars, 50 μm. Dot graphs show means ± SD of TH staining area normalized by prostatic stromal cell number. Each dot represents result from one mouse.

(D) Co-immunostaining of Krt14/AR in the AP of castrated and control adult C57BL/6 mice. Scale bars, 50 μm.

(E) Dot graphs show means ± SD of testosterone concentration in serum of the *Lgr5-DTR-EGFP* and control mice at day 9 after DT treatment and castrated adult C57BL/6 mice.
(F) Co-immunostaining of αSMA/TH in the AP of adult C57BL/6 mice at day 9 after 6-OHDA or saline treatment. Scale bars, 50 μm. Dot graphs show means ± SD of TH staining area normalized by prostatic stromal cell number. Each dot represents result from one mouse.
(G) Dot graphs show means ± SD of prostate weight of AP, DLP, and VP of 6-OHDA-treated and control mice. Each dot represents result from one mouse.
(H) Co-immunostaining of Krt8/Krt5 in the AP of 6-OHDA-treated and control mice. Scale bars, 50 μm.
(I) Co-immunostaining of Krt5/Ki67 in the AP of 6-OHDA-treated and control mice. Scale bars, 50 μm. Dot graphs show means ± SD of percentage of $Ki67^+$ epithelial cells. Each dot represents the result from one mouse.
(J) Co-immunostaining of Krt5/Krt8/cleaved casp 3 in the AP of 6-OHDA-treated and control mice. Scale bars, 50 μm. Dot graphs show means ± SD of percentage of cleaved $casp\ 3^+$ epithelial cells. Each dot represents result from one mouse.

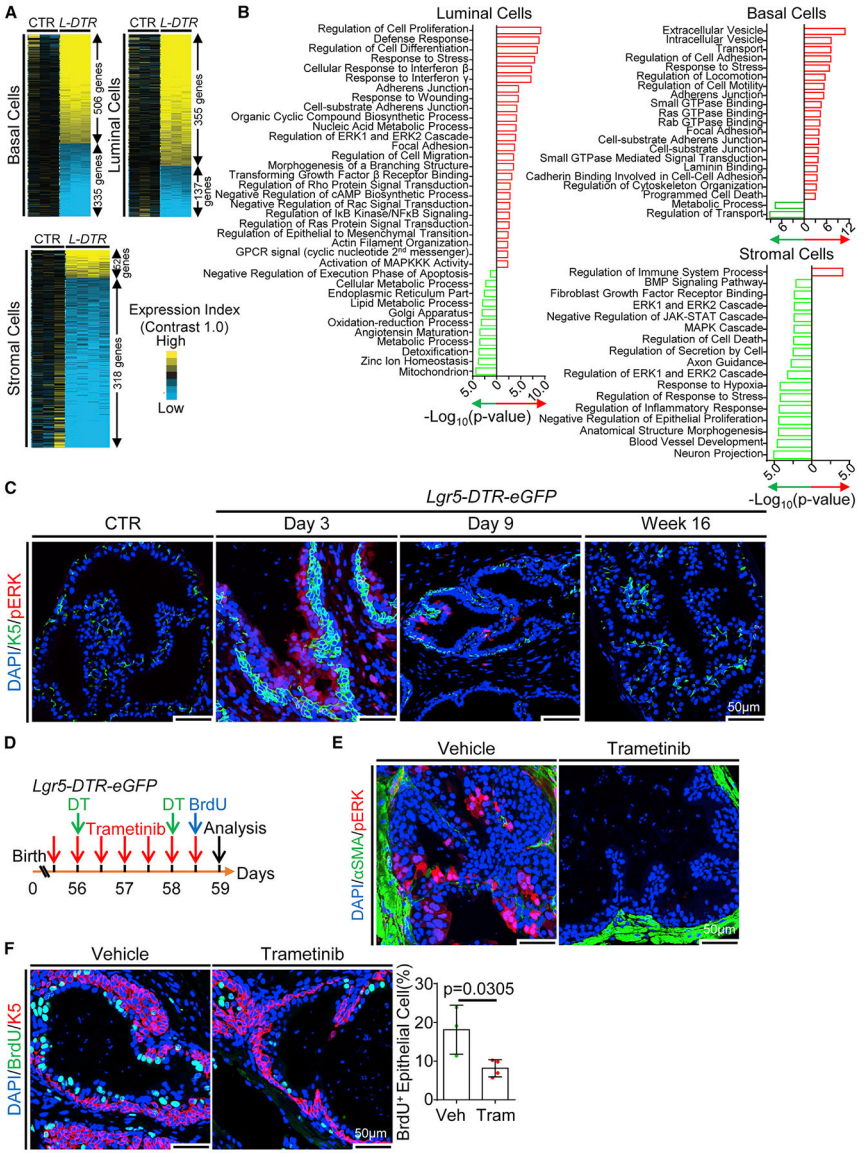

Figure 6. Molecular alterations induced by the ablation of Lgr5^{+} stromal cells

(A) Heatmaps of RNA-seq analysis of FACS-isolated basal, luminal, and stromal cells from *Lgr5-DTR-EGFP* and control mice at day 9 after DT treatment.

(B) Gene Ontology analysis of RNA-seq of FACS-isolated basal, luminal, and stromal cells from DT-treated *Lgr5-DTR-EGFP* and control mice. Red bars: upregulated in *Lgr5-DTR-EGFP* mice; green bars: downregulated in *Lgr5-DTR-EGFP* mice.

(C) Co-immunostaining of Krt5/p-ERK in the AP of *Lgr5-DTR-EGFP* and control mice at day 3, day 9, and week 16 after DT treatment. Scale bars, 50 μm.

(D) Schematic illustration of experimental design.

(E) Co-immunostaining of αSMA/p-ERK in AP of DT-treated *Lgr5-DTR-EGFP* mice after administration of trametinib or vehicle. Scale bars, 50 μm.

(F) Co-immunostaining of BrdU/Krt5 in the AP of DT-treated *Lgr5-DTR-EGFP* mice after administration of trametinib or vehicle. Scale bars, 50 μm. Dot graphs show means ± SD of percentage of $BrdU^+$ epithelial cells. Each dot represents result from one mouse.

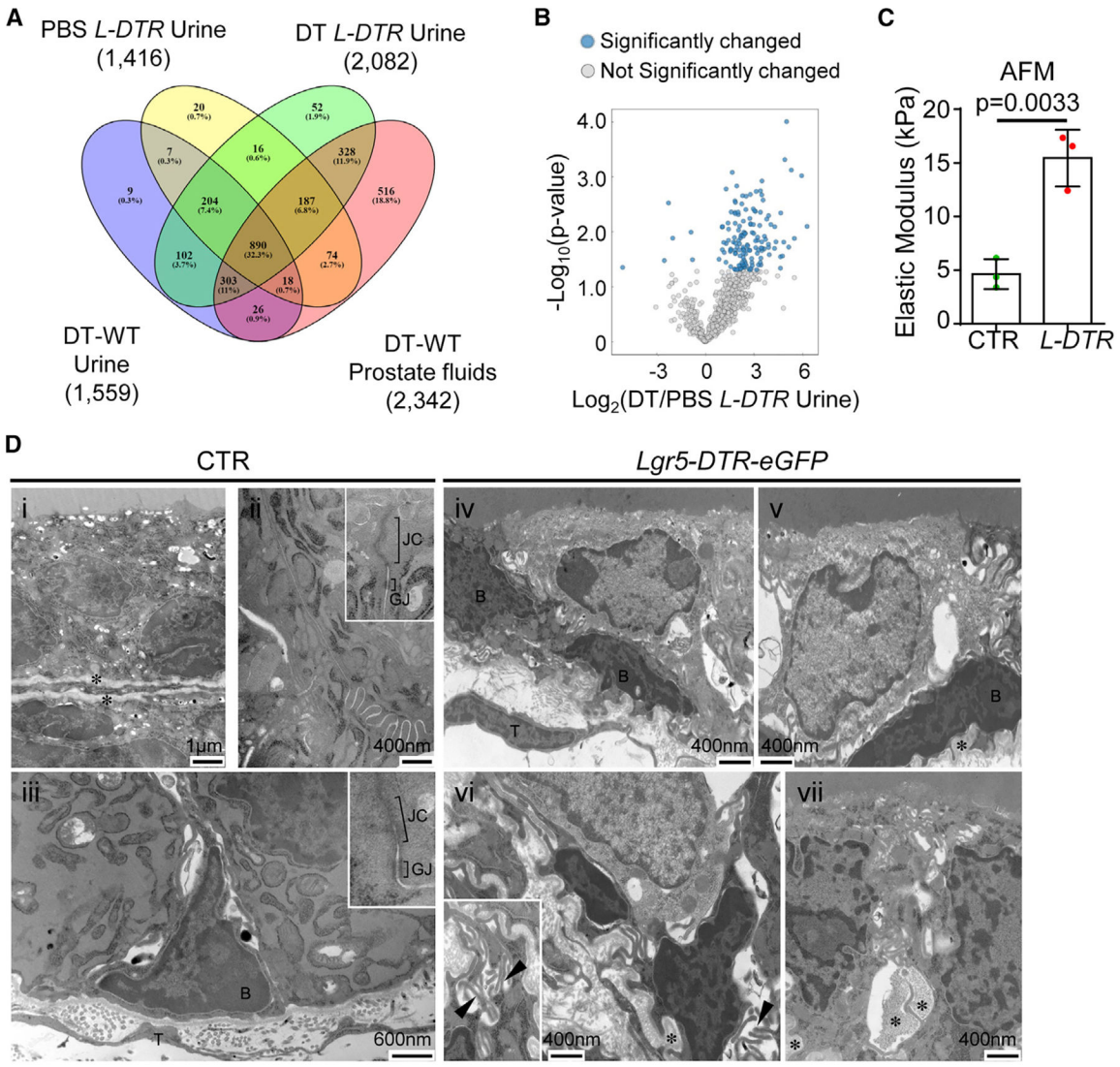

Figure 7. Ablating Lgr5^{+} stromal cells alters tissue rigidity

(A) Summary of protein identifications (after match-between-run) by liquid chromatography coupled to tandem mass spectrometry (LC-MS/MS) from prostate fluids and urine of DT-treated wild-type (WT) mice and urine of *Lgr5-DTR-EGFP* mice 9 days post PBS or DT treatment. The Venn diagram shows the number of overlapping proteins among the 4 groups.

(B) Quantitative proteomics analysis for the 1,077 proteins found in common in mouse prostate fluids and urine. Volcano plot shows significantly changed proteins in urine of DT-treated *Lgr5-DTR-EGFP* and control mice.

(C) Dot graphs show means ± SD of elastic modulus of the AP of *Lgr5-DTR-EGFP* and control mice at day 9 after DT treatment measured by atomic force microscopy (AFM). Each dot represents result from one mouse.

(D) Electron microscopy analysis of the AP of *Lgr5-DTR-EGFP* and control mice at day 9 after DT treatment. Luminal cells (i), cell adhesion complexes (ii), and basal cells (iii) in the control prostate. Disrupted architectural organization (iv and v), disrupted basement membrane and accumulation of electron dense material in the intercellular space (vi and vii),

and increased filopodia-like projections (vi) in the DT-treated *Lgr5-DTR-EGFP* prostate. Asterisks show the basement membranes. Arrowheads show the filopodia-like projections. JC, apical junctional complexes; GJ, gap junctions; B, basal cells; T, telocytes.

KEY RESOURCES TABLE

REAGENT or RESOURCE	SOURCE	IDENTIFIER
Antibodies		
Rat anti-BrdU (Clone BU1/75)	Abcam	Cat# ab6326; RRID: AB_305426
Rabbit anti-Mouse Nkx3.1	Athena Enzyme Systems	Cat# 0315
Chicken anti-GFP	Abcam	Cat# ab13970; RRID: AB_300798
Mouse anti-RFP (Clone RF5R)	Invitrogen	Cat# MA5–15257; RRID: AB_10999796
Rabbit anti-Mouse Vimentin	Cell Signaling Technology	Cat# 5741S; RRID: AB_10695459
Rat anti-Mouse Sca1 (Clone D7)	BD Pharmingen	Cat# 557403; RRID: AB_396686
Rabbit anti-Mouse CD31	Abcam	Cat# ab28364; RRID: AB_726362
Rat anti-Mouse CD45 (Clone 30-F11)	BD Pharmingen	Cat# 550539; RRID: AB_2174426
Rat anti-Mouse Ki67 (Clone SolA15)	Invitrogen	Cat# 14-5698-82; RRID: AB_10854564
Rabbit anti-Mouse AR	Santa Cruz Biotechnology	Cat# sc-816; RRID: AB_1563391
Rabbit anti-Mouse TH	Sigma-Aldrich	Cat# AB152
Mouse anti-Mouse K14 (Clone LL002)	Santa Cruz Biotechnology	Cat# sc-58724; RRID: AB_784170
Rabbit anti-Mouse K5 (Clone Poly19055)	BioLegend	Cat# 905504; RRID: AB_2616956
Chicken anti-Mouse K5 (Clone Poly9059)	BioLegend	Cat# 905904; RRID: AB_2721743
Mouse anti-Mouse K8 (Clone 1E8)	Covance	Cat# MMS-162P; RRID: AB_2565043
Rat anti-Mouse K8	Developmental Studies Hybridoma Bank	Cat# Troma-1; RRID: AB_531826
Mouse anti-Mouse Smooth Muscle Actin (Clone 1A4)	Sigma-Aldrich	Cat# 202M; RRID: AB_1157937
Rabbit anti-Mouse Cleaved Caspase 3	Cell Signaling Technology	Cat# 9661S; RRID: AB_2341188
Rabbit anti-Mouse phospho-ERK1/2 (Thr202/Tyr204) (Clone D13.14.4E)	Cell Signaling Technology	Cat# 4370S; RRID: AB_2315112
Rabbit anti-Mouse ERK1/2	Cell Signaling Technology	Cat# 9102S; RRID: AB_330744
Rabbit anti-Mouse phospho-JNK (Thr183/Tyr185)	Cell Signaling Technology	Cat# 4668T; RRID: AB_823588
Rabbit anti-Mouse JNK	Cell Signaling Technology	Cat# 9252T; RRID: AB_2250373
Rabbit anti-Mouse phospho-P38 MAPK (Thr180/Tyr182)	Cell Signaling Technology	Cat# 4511T; RRID: AB_2139682
Rabbit anti-Mouse P38 MAPK	Cell Signaling Technology	Cat# 9212S; RRID: AB_330713
Rabbit anti-Mouse phospho-cJun (Ser73)	Cell Signaling Technology	Cat# 9164L; RRID: AB_330892
Rabbit anti-Mouse phospho-FAK (Tyr397) (Clone 31H5L17)	Invitrogen	Cat# 700255; RRID: AB_2532307
Rabbit anti-Mouse FAK	Cell Signaling Technology	Cat# 3285T; RRID: AB_2269034
Rabbit anti-Mouse phospho-YAP (Ser127)	Cell Signaling Technology	Cat# 4911S; RRID: AB_2218913
Rabbit anti-Mouse YAP	Cell Signaling Technology	Cat# 4912S; RRID: AB_2218911
Rabbit anti-Mouse MKL1	Sigma-Aldrich	Cat# SAB4502519; RRID: AB_10746802
Rabbit anti-Mouse β-Catenin (Clone 6B3)	Cell Signaling Technology	Cat# 9582P; RRID: AB_823447
Rabbit anti-Mouse Gapdh (Clone 14C10)	Cell Signaling Technology	Cat# 2118S; RRID: AB_561053
Goat α-Mouse IgG(H+L) Alexa Fluor 488	Invitrogen	Cat# A11029; RRID: AB_2534088
Goat α-Mouse IgG(H+L) Alexa Fluor 594	Invitrogen	Cat# A11020; RRID: AB_2534087
Goat α-Rabbit IgG(H+L) Alexa Fluor 594	Invitrogen	Cat# A11037; RRID: AB_2534095

REAGENT or RESOURCE	SOURCE	IDENTIFIER
Goat α-Rat IgG(H+L) Alexa Fluor 488	Invitrogen	Cat# A11006; RRID: AB_2534074
Goat α-Rat IgG(H+L) Alexa Fluor 594	Thermo Fisher Scientific	Cat# A11007; RRID: AB_10561522
Goat α-Chicken IgY(H+L) DyLight 488	Abcam	Cat# ab96951; RRID: AB_10679800
Goat α-Mouse IgG(H+L) Alexa Fluor 633	Thermo Fisher Scientific	Cat# A21053; RRID: AB_2535720
Goat a-Rabbit IgG(H+L) HRP	Vector Lab.	Cat# PI-1000; RRID: AB_2336198
Rat anti-Mouse CD31-eFluor 450 (Clone 390)	eBioscience	Cat# 48-0311-82; RRID: AB_10598807
Rat anti-Mouse CD45-eFluor 450 (Clone 30-F11)	eBioscience	Cat# 48-0451-82; RRID: AB_1518806
Rat anti-Mouse Ter119-eFluor 450 (Clone TER-119)	eBioscience	Cat# 48-5921-82; RRID: AB_1518808
Rat anti-Mouse CD49f-APC (Clone eBioGoH3)	eBioscience	Cat# 17-0495-82; RRID: AB_2016694
Rat anti-Mouse Sca1-PE (Clone D7)	eBioscience	Cat# 12-5981-83; RRID: AB_466087
Rat anti-Mouse CD24-PECy7 (Clone M1/69)	BD Biosciences	Cat# 560536; RRID: AB_1727452
Rat anti-Mouse CD24-FITC (Clone M1/69)	eBioscience	Cat# 11-0242-85; RRID: AB_464989
Rat anti-Mouse CD11b-FITC (Clone M1/70)	eBioscience	Cat# 11-0112-85; RRID: AB_464936
Rat anti-Mouse F4/80-PECy7 (Clone BM8)	eBioscience	Cat# 25-4801-82; RRID: AB_469653
Rat anti-Mouse CD19-APC (Clone 6D5)	BioLegend	Cat# 115512; RRID: AB_313647
Armenian hamster anti-Mouse CD3e-PE (Clone 145–2C11)	eBioscience	Cat# 12-0031-83; RRID: AB_465497
Rat anti-Mouse CD4-PerCP Cy5.5 (Clone GK1.5)	BioLegend	Cat# 100434; RRID: AB_893324
Rat anti-Mouse CD8a-PECy7 (Clone 53–6.7)	eBioscience	Cat# 25-0081-82; RRID: AB_469584
Chemicals, peptides, and recombinant proteins		
Ethyl cinnamate	Alfa Aesar	Cat# A12906
10% neutral buffered formalin	Fisher HealthCare	Cat# 23–245684
Diphtheria toxin	Sigma-Aldrich	Cat# D0564
Tamoxifen	Sigma-Aldrich	Cat# T5648
BrdU	Sigma-Aldrich	Cat# B5002–5G
EdU	Sigma-Aldrich	Cat# 900584–50MG
6OHDA	Sigma-Aldrich	Cat# H4381–500MG
Trametinib	Selleckchem.com	Cat# S2673
Normal goat serum	Vector Laboratories	Cat# S-1000
NucBlue Fixed Cell ReadyProbes Reagent (DAPI)	Invitrogen	Cat# R37606
Immobilon Classico Western HRP Substrate	Millipore	Cat# WBLUC0100
5α-Androstan-17β-ol-3-one	Sigma-Aldrich	Cat# A8380-10G
Pluronic F127	Biotium	Cat# 59004
Pierce™ DTT (Dithiothreitol)	Thermo Fisher Scientific	Cat#: 20291
Iodoacetamide	Thermo Fisher Scientific	Cat#: A3221
Lysyl endopeptidase	FUJIFILM Wako	Cat#: 129-02541

REAGENT or RESOURCE	SOURCE	IDENTIFIER
Sequencing-grade modified trypsin	Promega	Cat#: V517
Critical commercial assays		
iClick™ EdU Andy Fluor™ 488 Imaging Kit	ABP Biosciences	Cat# A003
RNA-Scope 2.5 HD Detection Reagent Red Kit	Advanced Cell Diagnostics	Cat# 322360
NucleoSpin RNA Plus XS Kit	Macherey-Nagel	Cat# 740990.50
NucleoSpin RNA XS Kit	Macherey-Nagel	Cat# 740902
iScript™ Reverse Transcription Supermix for RT-qPCR	Bio-Rad	Cat# 1708841
iTaq™ Universal SYBR Green Supermix	Bio-Rad	Cat# 1725124
Quick Start™ Bradford 1x Dye Reagent	Bio-Rad	Cat# 5000205
Glutaraldehyde, 50% EM	Ted Pella Inc.	Cat# 18432
SMART-Seq™ v4 Ultra Low Input RNA Kit for Sequencing	Clontech Laboratories	Cat# 634888
Nextera XT DNA Library Preparation Kit	Illumina	Cat# FC-131–1024
S-Trap™ micro columns	ProtiFi	Cat#: CO2-micro-40
Pierce™ BCA Protein Assay Kit	Thermo Fisher Scientific	Cat#: 23225
Deposited data		
RNA-seq data of the FACS-isolated basal, luminal and stromal cells in the anterior prostate of DT-treated Lgr5-DTR-eGFP and control mice	This paper	GEO: GSE190938
Experimental models: Organisms/strains		
Mouse: C57BL/6	Charles River	Strain code: 027
Mouse: SCID/Beige	Charles River	Strain code: 250
Mouse: *Lgr5-DTR-eGFP*	Tian H et al. 2011	N/A
Mouse: *Krt7-CreER^{T2}*	Jiang M et al. 2017	N/A
Mouse: *Krt8-CreER^{T2}*	Zhang L et al. 2012	JAX stock #037269
Mouse: *Pdgfrβ-CreER^{T2}*	The Jackson Laboratory	JAX stock #029684
Mouse: *NG2-CreER^{T2}*	The Jackson Laboratory	JAX stock #008538
Mouse: *Col1a2-CreER^{T2}*	The Jackson Laboratory	JAX stock #029567
Mouse: *C57BU6-Gt(ROSA)26Sor$^{tm1(HBEGF)Awai}$/J*	The Jackson Laboratory	JAX stock #007900
Mouse: *B6.Cg-Gt(ROSA)26Sor$^{tm14(CAG-tdTomato)Hze}$/J*	The Jackson Laboratory	JAX stock #007914
Mouse: *B6.129P2-Lgr5$^{tm1(cre/ERT2)cle}$/J*	The Jackson Laboratory	JAX stock #008875
Mouse: *B6.Cg-Gt(ROSA)26Sor$^{tm3(CAG-EYFP)Hze}$/J*	The Jackson Laboratory	JAX stock #007903
Oligonucleotides		
Primers for genotyping of mouse lines, see Table S1	This paper	N/A
qPCR Primer: mouse *Lgr5* Forward: CAACCTCAGCGTCTTCACCT	This paper	N/A
qPCR Primer: mouse *Lgr5* Reverse: AAGCAGAGGCGATGTAGGAG	This paper	N/A
Software and algorithms		
Fiji	ImageJ	RRID: SCR_002285
BigStitcher	Hörl D etal. 2019	https://imagej.net/plugins/bigstitcher/
Aivia v8.5	DRVision Technologies LLC	N/A
Asylum Research force curve analysis software	Asylum Research	N/A
SigTerms	Creighton et al. 2008	http://sigterms.sourceforge.net/

REAGENT or RESOURCE	SOURCE	IDENTIFIER
Leica Application Suite X	Leica Microsystems GmbH	RRID:SCR_013673; https://www.leicamicrosystems.com/products/microscopesoftware/details/product/leica-las-x-ls/
STAR Galaxy Version 2.5	RNA STAR	https://biostar.galaxyproject.org/
R version 3.6	R Packages	https://r-pkgs.org/
TreeView 1.2.0	Java TreeView	http://jtreeview.sourceforge.net/
FlowJo	Tree Star	RRID:SCR_008520; https://www.flowjo.com/solutions/flowjo
GraphPad Prism 7	GraphPad Software	RRID:SCR_002798
MSFragger	PMID: 28394336	https://msfragger.nesvilab.org/
Perseus	PMID: 27348712	https://maxquant.net/perseus/
Other		
Nikon A1R confocal microscope	Nikon	N/A
Amersham Imager 600	GE Healthcare	N/A
Leica M165 FC Fluorescent Stereo Microscope	Leica	https://www.leica-microsystems.com/products/stereo-microscopes-macroscopes/p/leica-m165-fc/
Leica DM4 B Upright Digital Microscope	Leica	N/A